ARTICLE

Intrusion-related affinity and orogenic gold overprint at the Paleoproterozoic Bonikro Au–(Mo) deposit (Côte d'Ivoire, West African Craton)

Quentin Masurel[1] · Nicolas Thébaud[1] · Andrew Allibone[2] · Anne-Sylvie André-Mayer[3] · Kim A. A. Hein[4] ·
Laurie Reisberg[5] · Olivier Bruguier[6] · Aurélien Eglinger[3] · John Miller[7]

Abstract

The Bonikro gold deposit and satellite Hiré open pits are located at the southern tip of the Oumé-Féttékro granite–greenstone belt in Côte d'Ivoire. Country rocks in the region have undergone polyphase deformation and prolonged arc magmatism during the Paleoproterozoic Eburnean orogeny. Intrusive host rocks at Hiré and Bonikro have been dated at 2180 ± 6 and 2086 ± 4 Ma (U–Pb on zircon), respectively. These plutonic bodies acted as favourable sites for fluid flow due to their brittle rheological characteristics. Gold mineralisation at Bonikro is hosted by (i) a sheeted quartz vein array characterised by an Au–W–Bi–Te–Ag metal association, in the cupola of a porphyritic granodiorite; and (ii) an overprinting swarm of fault-fill smoky quartz–(molybdenite) veins. Gold mineralisation at Hiré is shear-hosted and shares a similar relative timing with the latter set of auriferous veins. This second phase of gold mineralisation occurred during a period of transcurrent tectonics late in the Eburnean tectono-magmatic history, soon after the cessation of compressional deformation. It is responsible for the bulk of gold resources in the region (e.g. Bonikro, Hiré, Agbahou) and has been dated at 2074 ± 16 Ma (Re–Os on molybdenite). The integration of structural–paragenetic relationships with high precision dating of magmatic and hydrothermal events highlights the superposition of late Eburnean orogenic gold mineralisation on an earlier intrusion-related gold system linked to the local emplacement of a porphyritic granodiorite at Bonikro and illustrates the genetic diversity of Paleoproterozoic granitoid-hosted gold mineralisation in the West African Craton. It also further supports that gold mineralisations in the West African Craton occurred diachronously throughout the Eburnean orogeny through a variety of deposit types including Au-skarn, intrusion-related Au, orogenic Au, and porphyry Cu–Au.

Keywords Bonikro · Eburnean orogeny · Orogenic gold · Intrusion-related gold

---

Editorial handling: P. Eilu

✉ Quentin Masurel
    qmasurel@hotmail.com

1   Centre for Exploration Targeting, The University of Western
     Australia, 35 Stirling Highway, Crawley, WA 6009, Australia

2   Rodinian Ltd, PO Box 758, Wanaka 9343, New Zealand

3   GeoRessources, Université de Lorraine – CNRS, Nancy 54000,
     France

4   University of the Witwatersrand, Johannesburg, Braamfontein 2001,
     South Africa

5   Centre de Recherche Pétrographiques et Géochimiques (CRPG),
     CNRS-Université de Lorraine, Vandoeuvre-lès-Nancy 54501, France

6   Geosciences Montpellier, Université Montpellier II,
     Montpellier 34090, France

7   Mineral Resources, Commonwealth Scientific and Industrial
     Research Organisation (CSIRO), Australian Resources Research
     Centre (ARRC), Kensington, WA 6151, Australia

Introduction

The majority of gold deposits in the West African Craton belong to the orogenic class and formed during the latter stages of the Eburnean orogeny between ca. 2100 and 2050 Ma (Béziat et al. 2008; Oberthür et al. 1998; Feybesse et al. 2006; Masurel et al. 2017c; Le Mignot et al. 2017b; Augustin et al. 2016). Intrusion-related (e.g. Morila, McFarlane et al. 2011; Hammond et al. 2011), porphyry (e.g. Gaoua, Le Mignot et al. 2017a, b) and skarn gold deposits (e.g. Ity, Béziat et al. 2016; Tongon, Lawrence et al. 2017) have also been described from the Paleoproterozoic terranes of West Africa. Granitoid-hosted gold deposits are a relatively recently recognised style of gold mineralisation in West Africa (e.g. Subika, Nhyiaso, Ayankyerim, Nyhiaso, Chirano, Ayanfuri, Amansie; Bonikro, Hiré, Kao and Nami). The role of granitoids in the genesis of gold-bearing mineral systems in complex and evolving

metamorphic belts remains debated. The host granitoids may have acted as favourable sites for fluid flow due to their brittle lithological characteristics (Allibone et al. 2002a, 2004; Feybesse et al. 2006), and/or a source of fluids and metals (Yao and Robb 2000; Yao et al. 2001; McFarlane et al. 2011). Much of the debate concerning the source of fluids and metals for granitoid-hosted gold systems in West Africa lies in the fact that both melts and metal-bearing fluids were products of the same deep-crustal or mantle-generated thermal event during the late Eburnean orogeny (Feybesse et al. 2006; Lambert-Smith et al. 2016; Eglinger et al. 2017). Granitoid-hosted gold mineralisation in the Bonikro–Hiré district (Ouatarra 2015) provides a good opportunity to investigate the genetic link, if any, between Eburnean plutonism and gold mineralisation. In this study, we integrate structural and mineral paragenetic relationships with high precision U–Pb dating of magmatic zircons and Re–Os dating of hydrothermal molybdenite to establish temporal relationships between pluton emplacement, deformation and gold mineralisation. We then propose a genetic model for the granitoid-hosted Bonikro–Hiré gold system that further highlights the diversity of gold deposits within the Paleoproterozoic terranes of West Africa (Goldfarb et al. 2017).

Regional geology

The Paleoproterozoic Baoulé-Mossi domain, in the southern part of the West African Craton, consists of linear to arcuate belts of volcano-sedimentary rocks, intra-orogenic sedimentary basins and intervening tonalite–trondjhemite–granodiorite plutonic terranes (Fig. 1) (Feybesse et al. 2006; Vidal et al. 2009). The Sassandra Fault (Bessoles 1977; Feybesse et al. 1989; Feybesse and Milési 1994) marks the boundary between the Archean Kénéma-Man domain to the west and the Paleoproterozoic terranes of the Baoulé-Mossi domain to the east.

The oldest volcanic rocks within the Baoulé-Mossi domain consist of tholeiitic basalts (Abouchami et al. 1990; Boher et al. 1992; Hirdes et al. 1996; Pouclet et al. 1996). Although the timing of the onset of this tholeiitic volcanism remains unconstrained, it transitioned into calc-alkaline intermediate volcanism between ca. 2200 and 2180 Ma (Sylvester and Attoh 1992; Dia et al. 1997; Baratoux et al. 2011; Pouclet et al. 2006). Voluminous tonalite, trondjhemite and granodiorite were emplaced between ca. 2190 and 2130 Ma within both the volcano-sedimentary belts and intervening plutonic terranes (Doumbia et al. 1998; Gasquet et al. 2003; Vidal et al. 2009; Parra-Avila et al. 2017). One or more periods of deformation and low- to high-grade metamorphism affected the Baoulé-Mossi domain during the Eoeburnean Orogeny between ca. 2180 and 2140 Ma (Hein 2010; Perrouty et al. 2012; Tshibubudze and Hein 2013; McCuaig et al. 2016; Block et al. 2016; Augustin et al. 2017). Scattered VMS

(e.g. Perkoa, Schwartz and Melcher 2003), porphyry Cu (e.g. Gaoua, Le Mignot et al. 2017a, 2017b) and minor orogenic gold deposits (e.g. Wassa, Parra-Avila et al. 2015; Perrouty et al. 2016; and Kiaka, Fontaine et al. 2017) formed during this time period.

Diachronous periods of extension and basin development throughout much of West Africa began at ca. 2135 Ma in the east and ca. 2120 Ma in the west of the Baoulé-Mossi domain, respectively (Davis et al. 1994; Oberthür et al. 1998; Hirdes and Davis 2002; Adadey et al. 2009; Lebrun et al. 2016). Thick sequences of siliciclastic rocks deposited in deep water environments filled these basins, although shallower water rock sequences that included evaporites and impure limestones were deposited locally (e.g. Siguiri Series in Guinea, Leube et al. 1990; Lebrun et al. 2016; and the Kofi Series in Mali, Lambert-Smith et al. 2016). High-grade metamorphic rocks, including migmatites and ortho- and para-gneisses, were locally unroofed during this period of intra-orogen extension (Block et al. 2016).

These basins were subsequently inverted and metamorphosed between ca. 2120–2115 and 2110–2100 Ma in the eastern and western parts of the Boulé-Mossi domain, respectively (Oberthür et al. 1998; Feybesse et al. 2006; Lebrun et al. 2016). Contractional deformation was coeval with emplacement of calc-alkaline K-feldspar- and biotite-bearing granodiorite and granite plutons (Oberthür et al. 1998; Parra-Avila et al. 2017). Progressive deformation and basin inversion led to the local deposition of syn-orogenic molasse within basins along major fault systems, such as the Tarkwa (Pigois et al. 2003; Perrouty et al. 2012) and Bui series (Zitsmann et al. 1997). Wassa-type gold deposits, formed before ca. 2140 Ma during the Eoeburnean Orogeny, are inferred to have been the source of gold within the Tarkwaian paleoplacers in the Ashanti belt of Ghana (Goldfarb et al. 2017).

Fold-and-thrust tectonics switched to widespread transcurrent tectonics after ca. 2100 Ma, coeval with regional greenschist-facies metamorphism (Feybesse et al. 2006; Baratoux et al. 2011; Lebrun et al. 2017; Masurel et al. 2017c). Voluminous high-K granitoids and biotite–muscovite–leucogranites were emplaced between ca. 2100 and 2060 Ma (Eglinger et al. 2017; Parra-Avila et al. 2017; Masurel et al. 2017a, b, c), after the onset of transcurrent deformation. Tectono-thermal activity continued until ca. 2050 Ma in the western and southern parts of the Boulé-Mossi domain after ceasing at ca. 2095 Ma in its northeastern part (Parra-Avila et al. 2017). Most gold deposits, including all the + 5 Moz deposits discovered to date in the Baoulé-Mossi domain, formed between ca. 2100 and 2060 Ma (Goldfarb et al. 2017), making this the most significant period of gold metallogenesis in West Africa. Although the majority of these gold deposits have characteristics typical of orogenic gold deposits (e.g. Obuasi, Allibone et al. 2002a; Fougerouse et al. 2017; Bogoso, Allibone et al. 2002b; Chirano,
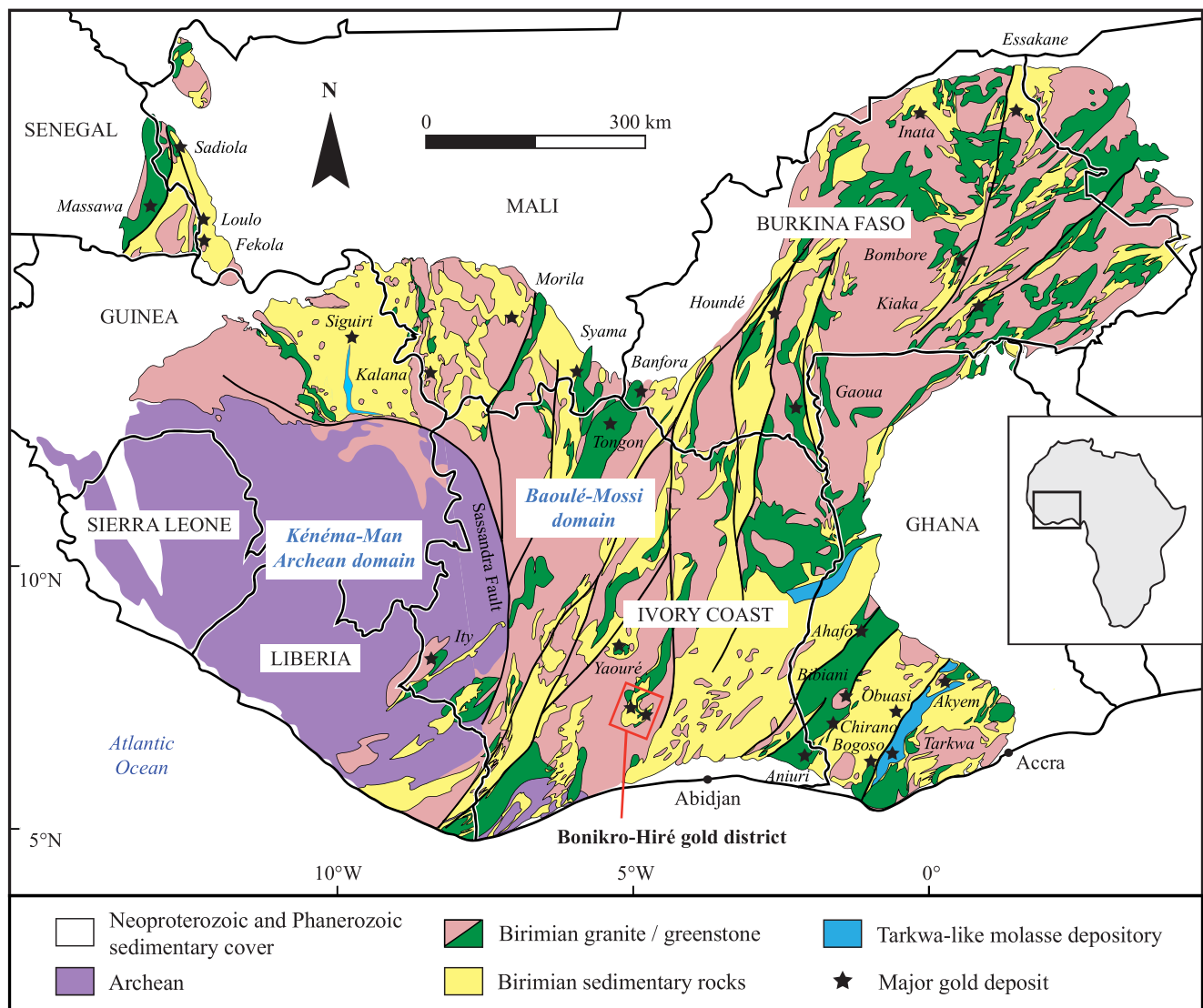
Fig. 1 Geological map of the southern part of the West African Craton (modified after Milési et al. 2004) showing the location of the Bonikro–Hiré gold district in Côte d'Ivoire

Allibone et al. 2004; Siguiri, Lebrun et al. 2016; Mana, Augustin et al. 2017) others have, at least in part, a magmatic affinity (e.g. Morila, McFarlane et al. 2011; Loulo, Lawrence et al. 2013a, b; Alamoutala, Masurel et al. 2017b).

Local geology

The Oumé-Féttékro Greenstone Belt (Yacé 1982; Lemoine 1988; Olson 1989; Mortimer 1990; Leake 1992; Daouda 1998) is located in south-central Côte d'Ivoire (Fig. 1). The greenstone belt extends ~ 300 km along strike, parallel to the NNE–SSW-trending regional structural grain. The southern part of the greenstone belt includes the Bonikro, Hiré and Agbahou gold deposits (Fig. 2). The south-central part of the Oumé-Féttékro Greenstone Belt, in the Bonikro district, consists of Toumodi Group supracrustal rocks and the Kan River

Plutonic Complex (Fig. 2), which consists of distinct suites of tonalite, trondhjemite and granodiorite as defined by Mortimer (1990). The Loukouyakro suite occupies most of the terrain and consists predominantly of tonalitic–trondhjemitic–granodioritic orthogneisses containing mafic enclaves and local migmatitic orthogneisses. The younger Diéri-Kouassikro suite occupies the western margin of the plutonic complex and consists predominantly of biotite-bearing trondhjemite. Intrusive rocks of these two suites occur as augen leuco-gneisses and banded orthogneisses within the deformation envelopes of the Boni-Andokro and Brobo shear zones. The youngest and minor component of the plutonic complex comprises isolated masses of amphibolite referred to as the Orumboboka suite, whose setting remains poorly constrained. The Kan River Plutonic Complex was interpreted as the mid- to lower-crustal remnant of a volcanic arc, metamorphosed and unroofed during the assembly of Baoulé-
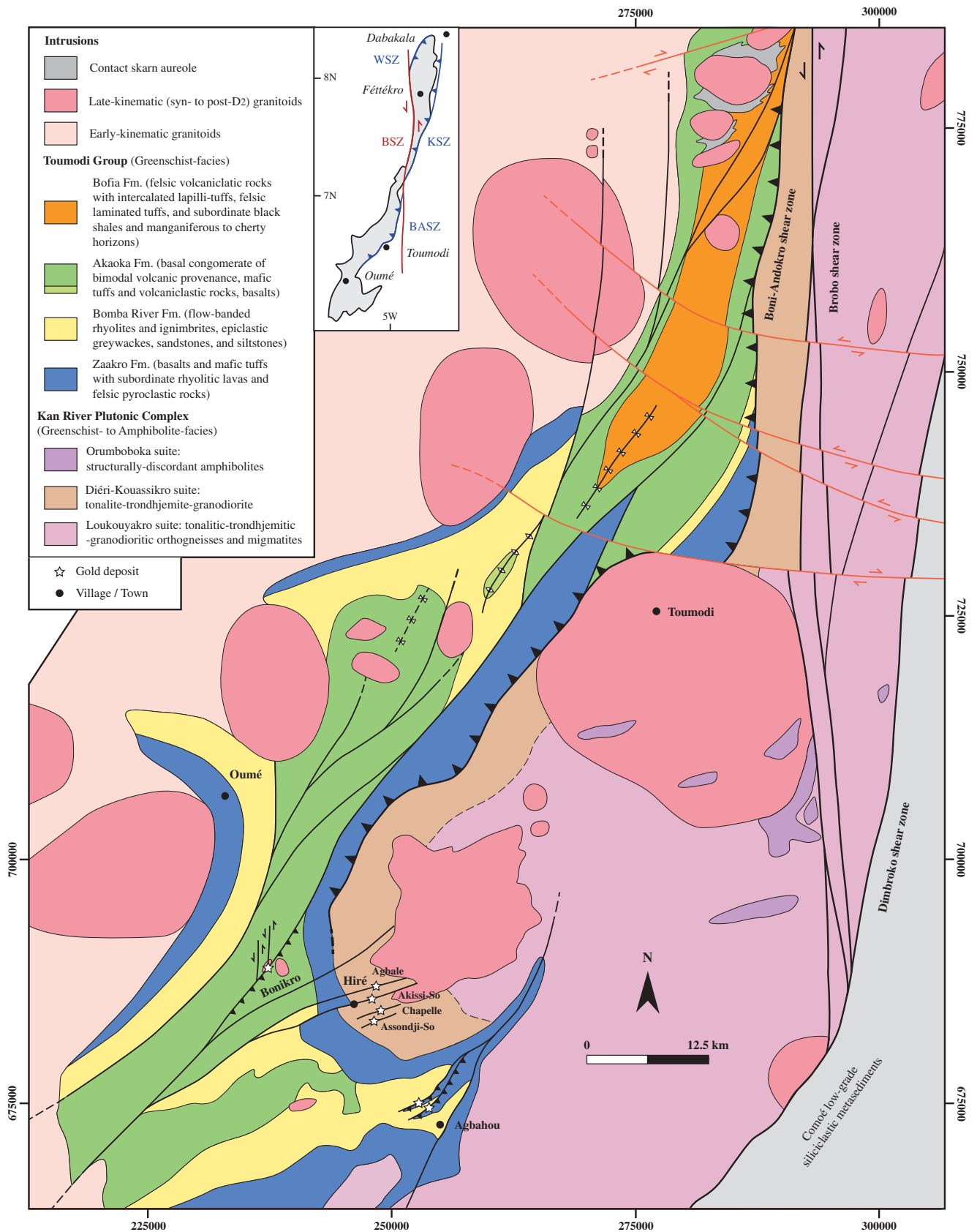
Fig. 2 Geology of the southern part of the Oumé-Féttékro greenstone belt (modified after Mortimer 1990, 2016). The inset shows the structural geometry of the belt (WSZ = Waléguéra shear zone, KSZ = Katédougou shear zone, BASZ = Boni-Andokro shear zone, BSZ = Brobo shear zone). The Bonikro, Hiré and Agbaou gold deposits are located at the southernmost end of the granite–greenstone belt

Mossi Domain (Mortimer 1990). Similar TTG-like plutonic rocks in the Dabakala area, in the northern part of the Oumé-Féttékro Greenstone Belt, were emplaced at ca. 2150 Ma (Lemoine 1988; Gasquet et al. 2003).

The Toumodi Group, in the Bonikro district, is divided into four lithostratigraphic formations, each less than 1500 m thick (Mortimer 1990, 1992a, b, 2016): (i) the basal Zaakro Fm., which comprises pillow basalts and mafic, lithic tuffs with subordinate rhyolite flows; (ii) the Bomba River Fm., which consists of epiclastic sandstones, flow-banded rhyolites and ignimbrites; (iii) the Akaoka Fm., which includes a basal epiclastic conglomerate overlain by mafic lithic tuffs and basalts with subordinate epiclastic sandstone horizons; and (iv) the top Bofia Fm., which comprises felsic volcaniclastic rocks, intercalated lapilli tuffs, laminated rhyolitic tuffs and minor discontinuous black shale, manganiferous and cherty horizons (Fig. 2). The Toumodi Group is inferred to have been deposited in an evolving volcanic arc, with the basal Zaakro Fm. representing its immature stage and the Bofia Fm. its most evolved stage (Mortimer 1990). Stratigraphic correlations across the Oumé-Féttékro Greenstone Belt, and limited geochronological data, suggest that the Bofia Fm. was deposited between ca. 2150 and 2100 Ma (Lemoine 1988; Mortimer 1990; Leake 1992). The interdigitation of lava flows and bimodal volcaniclastic and epiclastic rocks suggests that the Toumodi Group is a single volcano-sedimentary succession (Fig. 2). Numerous elliptical to circular calc-alkaline plutons of various sizes and compositions, such as the Toumodi granite, intruded the Toumodi Group and Kan River Plutonic Complex after ca. 2100 Ma (Fig. 2). The metamorphic mineral assemblages in the Toumodi Group generally include chlorite–epidote–sericite ± biotite–actinolite–calcite, indicative of regional greenschist-facies metamorphic conditions (Houssou 2013; Ouatarra 2015). Amphibolite-facies mineral assemblages are locally present in the Toumodi Group adjacent to some granitoid plutons (Ouatarra 2015).

Polyphase deformation has affected the south-central part of the Oumé-Féttékro Greenstone Belt (Lemoine 1988; Mortimer 1990; Leake 1992; Houssou 2013; Ouatarra 2015). Early D_1 WNW–ESE-directed compression resulted in the formation of tight to isoclinal, N- to NNE-trending, gently plunging folds (F_1), and a penetrative axial–planar cleavage (S_1). Incremental bulk deformation during D_2 WNW–ESE-directed shortening resulted in the formation of the regional-scale Boni-Andokro shear zone and eastwards-directed thrusting of the Toumodi Group over the Kan River Plutonic Complex (Fig. 2). Higher-order, steeply dipping shear zones and back-thrusts also formed during D_2 shortening. The NNE-trending structural grain of the Bonikro district is a result of D_1 and D_2 deformation. NW–SE-directed shortening during D_3 resulted in the development of N to NNE-striking, brittle-ductile, sinistral shear zones such as the regional-scale Brobo Shear Zone, and reactivation of the older

structures such as the Boni-Andokro Shear Zone (Lemoine 1982; Mortimer 1990, 1992a) (Fig. 2). E–W-directed shortening during D_4 resulted in the development of conjugate ENE-striking dextral and WNW-striking sinistral brittle strike-slip faults (Fig. 2).

Most gold mineralisation in the Bonikro–Hiré and Agbahou area is interpreted to have occurred during D_3 sinistral and/or sinistral-reverse displacement along high-order N-to NE-trending brittle-ductile shear zones (Houssou 2013; Ouatarra 2015). Gold mineralisation is hosted in granitoids at Bonikro and Hiré and in basalts at Agbahou. The Agbahou gold deposit (Houssou 2013; Houssou et al. 2017) is an example of a vein-hosted greenstone gold deposit (Robert and Poulsen 2001; Dubé and Gosselin 2007). In contrast, Au–(Mo) mineralisation at Bonikro, first documented by Ouatarra (2015), has been interpreted to have a magmatic affinity.

Mining background

Bonikro village is located 250 km NW of Abidjan and 12 km SE of Hiré in Côte d'Ivoire. The terrain in the Bonikro area is flat, at an average elevation of 215 m above sea level, and overlain by a weathering profile up to 60 m thick. Consequently, fresh unoxidised outcrops are scarce. Although the region displays widespread evidence of ancient and recent artisanal mining (Newcrest Mining Ltd. 2016), gold mineralisation was only discovered at Bonikro in the 1990s by Equigold N.L., following a regional soil geochemistry campaign. The 1200 × 400 m soil Au anomaly at Bonikro correlates with the Bonikro porphyritic granodiorite pluton, and is associated with elevated Mo–W–(Bi–Pb–Ag) as well as Au (Paul Kitto, personal communication). As of December 2011, the total in situ mineral resource was estimated to contain ~ 2.9 Moz Au and reserves of ~ 1.1 Moz Au with ~350,000 oz of past production (Newcrest Mining Ltd. 2012). Although molybdenite is present in subeconomic quantities at Bonikro, it was never considered for mining as a by-product (Ouatarra 2015). The Bonikro open pit was placed under care and maintenance in October 2015.

Materials and methods

Open pit mapping and diamond drill core logging

This study is based on mapping all accessible benches in the Bonikro open pit mine in both 2010 and 2016. Bench mapping at Hiré could only be conducted at the Chapelle and Akissi-So open pits during the earliest stage of mining when both pits were still exploiting saprolite ore. Mapping was complemented by geological logging of 30 diamond drill

holes chosen to include the main structural, lithological and mineralogical variations within the deposits. All structural readings are given in true north coordinates. Planar features are recorded as strike/dip/quadrant, whereas linear data are given as plunge and azimuth. In this paper, the "D_b" and "D_h" subscripts refer to deformation events in the Bonikro and Hiré gold deposits, respectively, but may differ from regional structural compilations reported elsewhere in the West African Craton.

Petrography and mineral chemistry

A total of 52 polished thin sections were studied using optical microscopy, scanning electron microscopy (SEM) and electron probe microanalysis (EPMA) at the University of Western Australia (Perth, Australia). Backscattered electron (BSE) imaging and mineral chemistry analyses were obtained using a Tescan Vega3 XM SEM equipped with an Oxford instrument X-ACT energy-dispersive spectrometer and a JEOL JXA-8530F Hyperprobe EPMA fitted with five wavelength-dispersive spectrometers. Quantitative microanalyses were performed using internal proprietary standards. The analytical software used to collect semi-quantitative microanalytical data was the Oxford Instruments® INCA analytical suite on the Tescan Vega 3. Operating parameters for the SEM-EDS include an accelerating voltage of 20 kV, a working distance of 15 mm, a beam current of 1.5 nA and a detector process time of 4 s. Operating conditions for EPMA analysis included an accelerating voltage of 20 kV, a beam current of 40 nA and a counting time of 40 s on peak for sulfides.

Geochronology

U, Th and Pb analyses on zircons from the Bonikro porphyritic granodiorite were performed by laser ablation inductively coupled plasma mass spectrometry (LA-ICP-MS) at the Université de Montpellier (France). Laser ablation was conducted using a Thermofinnigan Element XR mass spectrometer coupled to a Lambda Physik COMpex 102 excimer laser. Standard operating conditions described in Bosch et al. (2011) were used and include a spot size of 26 μm and an energy density of 12 J/cm^2 at a frequency of 4 Hz. The U/Pb and Pb/Pb isotopic ratios of unknowns were calibrated against the reference zircon material G91500 (Wiedenbeck et al. 1995). Data reduction was carried out using the software Glitter (Van Achterberg et al. 2001) and Isoplot (Ludwig 2003, 2009). Zircon reference material GJ1 (Jackson et al. 2004) was analysed twice after each round of five unknowns and provided a $^{206}Pb/^{238}U$ age of 605.2 ± 4.9 Ma ($n = 8$). Such age is within error of the reference value quoted in Jackson et al. (2004). Reproducibility of the G91500 zircon standard Pb/U and Pb/Pb ratios during the session were of ± 1.3 and $\pm 0.4\%$, respectively ($n = 12$). These uncertainties were added in

quadrature with the counting error to determine uncertainties of the individual Pb/U and Pb/Pb analyses. Raw U–Pb data is given in Table 1. The age is quoted at the 2σ confidence level.

U, Th and Pb analyses of zircons from the Hiré granodiorite were performed using the sensitive high-resolution ion microprobe (SHRIMP II) at the John de Laeter Centre of Excellence for Mass Spectrometry of Curtin University in Perth, Australia. Geochronological data were collected using standard operating procedures similar to those described by Compston et al. (1984) and Wingate and Kirkland (2013). Operating parameters include a 10-keV primary O^{2-} beam focussed to a ~20-μm diameter spot, a net primary ion current between 1.6 and 3.0 nA and a secondary ion analyser set to a mass resolution of ≥ 5000. Six data collection cycles (scans) were performed per analysis, and count times (per scan) were 10 s for the ^{204}Pb, ^{206}Pb and ^{208}Pb mass peaks and background and 30 s for the ^{207}Pb mass peak. The U/Pb and Pb/Pb isotopic ratios of unknowns were calibrated against the reference zircon materials M257 (561.3 Ma; Nasdala et al. 2008) and OGC1 (3465 Ma; Stern et al. 2009). Data reduction was carried out using the software Squid and Isoplot (Ludwig 2003, 2009). Twenty-two analyses have been performed on 22 individual zircons over two sessions and corrected independently. Raw U–Pb data is given in Table 1. Analyses 1 to 17 were obtained together with 12 analyses of the M257 standard, which indicated a reproducibility of $\pm 0.95\%$. Analyses 18 to 22 were obtained together with 11 analyses of the M257 standard, which indicated a reproducibility of $\pm 1.87\%$. Calibration uncertainties were included in the calculated uncertainties of individual Pb/U and Pb/Pb analyses. Common-Pb corrections were applied to all analyses using contemporaneous isotopic compositions determined according to the model of Stacey and Kramers (1975). The resulting ages are quoted at the 2σ confidence level.

Two molybdenite samples were collected for Re–Os dating at the Centre de Recherches Pétrographiques et Géologiques in Nancy, France. Sample Mo-1 is from a fault-fill smoky quartz vein and constrains the age of high-grade gold mineralisation during D_{3b}. The second sample Mo-2 is from a late cross-fault and constrains the minimum age for gold mineralisation at Bonikro, post-D_{3b}. Early gold mineralisation associated with the sheeted quartz veins in the cupola of the porphyritic granodiorite remains undated. Analytical techniques applied in this study are based on those described by Shirey and Walker (1995) for sample digestion, using an Anton Paar HPA-S high pressure asher, and Birck et al. (1997) for osmium extraction. For each sample, ~ 100 mg of molybdenite powder was spiked with precisely weighed quantities of a mixed ^{185}Re–^{190}Os tracer solution and digested in a mixture of hydrochloric acid (2 mL), nitric acid (5 mL) and hydrogen peroxide (0.1 mL) at 300 °C for 3 h, under a pressure of 100 bars. After sample digestion, Os was separated by liquid–liquid extraction into liquid bromine. The Br_2 was then

Table 1 Geochronological data for the Bonikro porphyritic granodiorite (LA-ICP-MS) and the Chapelle granodiorite (SHRIMP)

Sample_ID	Pb* (ppm)	Th (ppm)	U (ppm)	Th/U	208Pb/206Pb	207Pb/206Pb	± (1 s)	207Pb/235U	± (1 s)	206Pb/238U	± (1s)	Rho	Apparent ages (Ma) 206Pb/238U	± (1 s)	207Pb/206Pb	± (1 s)	Conc. (%)
Bonikro porphyritic granodiorite																	
#1-1	107	145	226	0.64	0.198	0.1286	0.0006	6.6343	0.1088	0.3740	0.0059	0.95	2048	27	2079	9	98.5
#1-2	75	171	159	1.07	0.283	0.1290	0.0007	6.6343	0.1672	0.3686	0.0092	0.97	2023	43	2084	10	97.1
#1-3	69	65	148	0.44	0.144	0.1293	0.0007	6.5554	0.1101	0.3842	0.0058	0.94	2096	27	2089	10	100.3
#2-1	40	72	114	0.63	0.190	0.1301	0.0007	6.8515	0.2086	0.2979	0.0115	0.99	1681	57	2100	10	80.1
#3-1	79	78	175	0.45	0.138	0.1289	0.0007	5.3457	0.1109	0.3840	0.0059	0.95	2095	27	2083	9	100.6
#4-1	58	99	121	0.82	0.247	0.1302	0.0010	7.1528	0.0677	0.3985	0.0024	0.63	2162	11	2101	13	102.9
#6-1	122	153	260	0.59	0.180	0.1291	0.0006	6.8374	0.0456	0.3841	0.0017	0.68	2095	8	2086	9	100.4
#7-1	127	166	274	0.60	0.183	0.1291	0.0007	6.8385	0.0605	0.3841	0.0027	0.80	2095	13	2086	9	100.4
#8-1	84	100	182	0.55	0.156	0.1293	0.0007	7.0288	0.0796	0.3941	0.0039	0.88	2142	18	2089	10	102.5
#9-1	123	231	246	0.94	0.282	0.1293	0.0007	6.6713	0.0610	0.3742	0.0027	0.78	2049	13	2088	10	98.1
#10-1	100	137	223	0.61	0.175	0.1296	0.0007	6.6831	0.0576	0.3740	0.0025	0.76	2048	12	2092	10	97.9
#11-1	65	71	135	0.52	0.159	0.1299	0.0009	6.8833	0.1607	0.3843	0.0086	0.96	2096	40	2097	11	100.0
#12-1	80	100	181	0.55	0.157	0.1288	0.0007	6.6423	0.0535	0.3741	0.0022	0.74	2048	10	2082	9	98.4
#13-1	63	103	140	0.74	0.187	0.1293	0.0007	6.8443	0.1067	0.3840	0.0056	0.93	2095	26	2088	10	100.3
#14-1	53	58	122	0.47	0.132	0.1280	0.0007	6.8396	0.0609	0.3874	0.0027	0.77	2111	12	2071	10	101.9
#15-1	162	484	371	1.53	0.427	0.1293	0.0007	6.9084	0.0550	0.3875	0.0023	0.74	2111	11	2089	9	101.1
#16-1	109	118	242	0.49	0.147	0.1286	0.0006	6.4580	0.0569	0.3642	0.0026	0.82	2002	12	2079	9	96.3
#17-1	55	112	128	0.88	0.241	0.1303	0.0007	6.5534	0.1522	0.3648	0.0082	0.97	2005	39	2102	10	95.4
#18-1	79	104	182	0.57	0.162	0.1291	0.0007	7.1012	0.0661	0.3991	0.0030	0.82	2165	14	2085	9	103.8
Chapelle granodiorite																	
D2613-22		238	314	0.78	0.365	0.1394	0.93	8.13	2.3	0.423	2.1	0.91	2274	40	2219	16	102.9
D2613-18		171	345	0.51	0.141	0.1360	0.44	7.53	2.1	0.402	2.1	0.98	2177	38	2177	8	100.0
D2613-5		105	231	0.47	0.132	0.1357	0.50	7.49	1.3	0.401	1.2	0.92	2172	22	2173	9	99.9
D2613-23		156	237	0.68	0.191	0.1354	0.52	7.40	2.2	0.396	2.1	0.97	2153	39	2170	9	99.1
D2613-3		106	222	0.49	0.138	0.1361	0.51	7.44	1.3	0.397	1.2	0.92	2154	22	2178	9	98.7
D2613-10		102	178	0.59	0.169	0.1360	0.59	7.32	1.4	0.390	1.2	0.90	2124	23	2177	10	97.1
D2613-15		45	127	0.37	0.104	0.1361	0.69	7.30	1.5	0.389	1.3	0.89	2117	24	2179	12	96.7
D2613-14		60	171	0.36	0.103	0.1374	0.59	7.35	1.4	0.388	1.3	0.91	2115	23	2194	10	95.8
D2613-7		37	91	0.42	0.122	0.1358	0.86	7.19	1.7	0.384	1.5	0.86	2094	26	2175	15	95.6
D2613-17		156	329	0.49	0.139	0.1376	0.44	7.35	1.2	0.387	1.1	0.93	2110	21	2198	8	95.3
D2613-21		103	155	0.69	0.191	0.1358	0.61	7.13	2.3	0.381	2.2	0.96	2081	40	2174	11	95.0
D2613-12		95	217	0.45	0.135	0.1374	0.52	7.21	1.3	0.381	1.2	0.92	2080	22	2194	9	93.9

Table 1 (continued)

Sample_ID	Pb* (ppm)	Th (ppm)	U (ppm)	Th/U	^{208}Pb/^{206}Pb	^{207}Pb/^{206}Pb	± (1 s)	^{207}Pb/^{235}U	± (1 s)	^{206}Pb/^{238}U	± (1s)	Rho	Apparent ages (Ma) ^{206}Pb/^{238}U	± (1 s)	^{207}Pb/^{206}Pb	± (1 s)	Conc. (%)
D2613-1		53	140	0.39	0.128	0.1415	0.66	7.62	1.5	0.391	1.3	0.89	2125	24	2246	11	93.7
D2613-6		99	222	0.46	0.145	0.1390	0.62	7.34	1.3	0.383	1.2	0.89	2090	21	2215	11	93.4
D2613-16		57	182	0.32	0.102	0.1396	0.65	7.37	1.4	0.383	1.2	0.89	2098	22	2223	11	93.0
D2613-2		81	183	0.46	0.124	0.1381	0.56	7.18	1.4	0.377	1.2	0.91	2063	22	2203	10	92.6
D2613-4		58	154	0.39	0.114	0.1365	0.65	6.90	1.4	0.367	1.3	0.89	2013	22	2184	11	90.9
D2613-13		144	235	0.63	0.182	0.1372	0.52	6.95	1.3	0.367	1.2	0.92	2016	21	2192	9	90.7
D2613-24		60	156	0.40	0.119	0.1341	0.78	6.61	2.4	0.358	2.2	0.94	1971	38	2152	14	90.2
D2613-9		144	260	0.45	0.148	0.1364	0.55	6.67	1.3	0.355	1.2	0.90	1959	20	2181	10	88.2
D2613-11		75	191	0.40	0.158	0.1375	0.63	6.40	1.4	0.338	1.2	0.89	1875	20	2197	11	83.2
D2613-8		88	186	0.49	0.231	0.1412	0.85	6.37	1.5	0.327	1.2	0.82	1824	19	2242	15	78.6

evaporated and the osmium fraction was purified by microdistillation (Birck et al. 1997). The Re was extracted from the residual acidic solution by anion exchange using chromatographic columns (AG1 X8 resin). Re isotopic compositions for isotope dilution calculations were measured using an X-Series II quadrupole ICPMS. Instrumental mass fractionation during measurements was regularly monitored and corrected for using a 7-ppb Re standard. The Os samples were loaded on platinum filaments for analysis by negative thermal ionisation mass spectrometry (N-TIMS; Creaser et al. 1991; Völkening et al. 1991), using a Finnigan MAT 262 instrument. About 0.2 μL of a saturated solution of Ba(OH)$_2$ in 0.1 N NaOH (Birck et al. 1997) was added to the samples to maximise OsO$_3^-$ emission in the instrument. Analyses were made by peak jumping and ion counting using an ETP electron multiplier. Instrumental mass fractionation was corrected iteratively off-line by assuming that the true ^{192}Os/^{188}Os ratio of the sample loaded on the filament lay on a mixing line between the spike (5.00736) and natural (3.08271) values. The oxygen isotope composition determined by Nier (^{17}O/^{16}O = 0.0003708 and ^{18}O/^{16}O = 0.002045) was used to correct for isobaric interferences from heavy oxides. Common Os, including both the natural component and any contribution from the analytical blank, was monitored using mass ^{188}Os, and a correction to ^{187}Os was applied assuming a common ^{187}Os/^{188}Os value of 0.5 ± 0.4. The magnitude of this correction was less than 0.01% for both samples studied. Although a Re blank measurement was not measured during these analyses, typical Re blank values in this laboratory are between 0.005 and 0.03 ng and, thus, are insignificant relative to the total quantities of Re (> 1000 ng) measured in these samples.

Results

Country rocks and their relationships to the porphyritic granodiorite at Bonikro

The Bonikro open pit is centred on a pluton of variably porphyritic to locally equigranular, granodiorite and subordinate tonalite (Figs. 3 and 4). Least-altered parts of the Bonikro porphyritic granodiorite comprise phenocrysts of oscillatory zoned plagioclase (25%), quartz (5%) and biotite (1–5%) in a quartzofeldspathic groundmass that includes accessory apatite, titanite and zircon but no primary Fe–Ti oxides. The eastern margin of this pluton cuts amygdaloidal to vesicular hornblende–pyroxene–phyric meta-basalts that are interlayered with 1–5 m thick units of bedded interflow sedimentary rocks. The western side of the pluton intrudes well-bedded volcaniclastic siltstones and mafic tuffs locally interbedded with 5–25 m thick basalt flows. Metamorphosed basaltic rocks east of the porphyritic granodiorite now comprise a mass of interlocking light
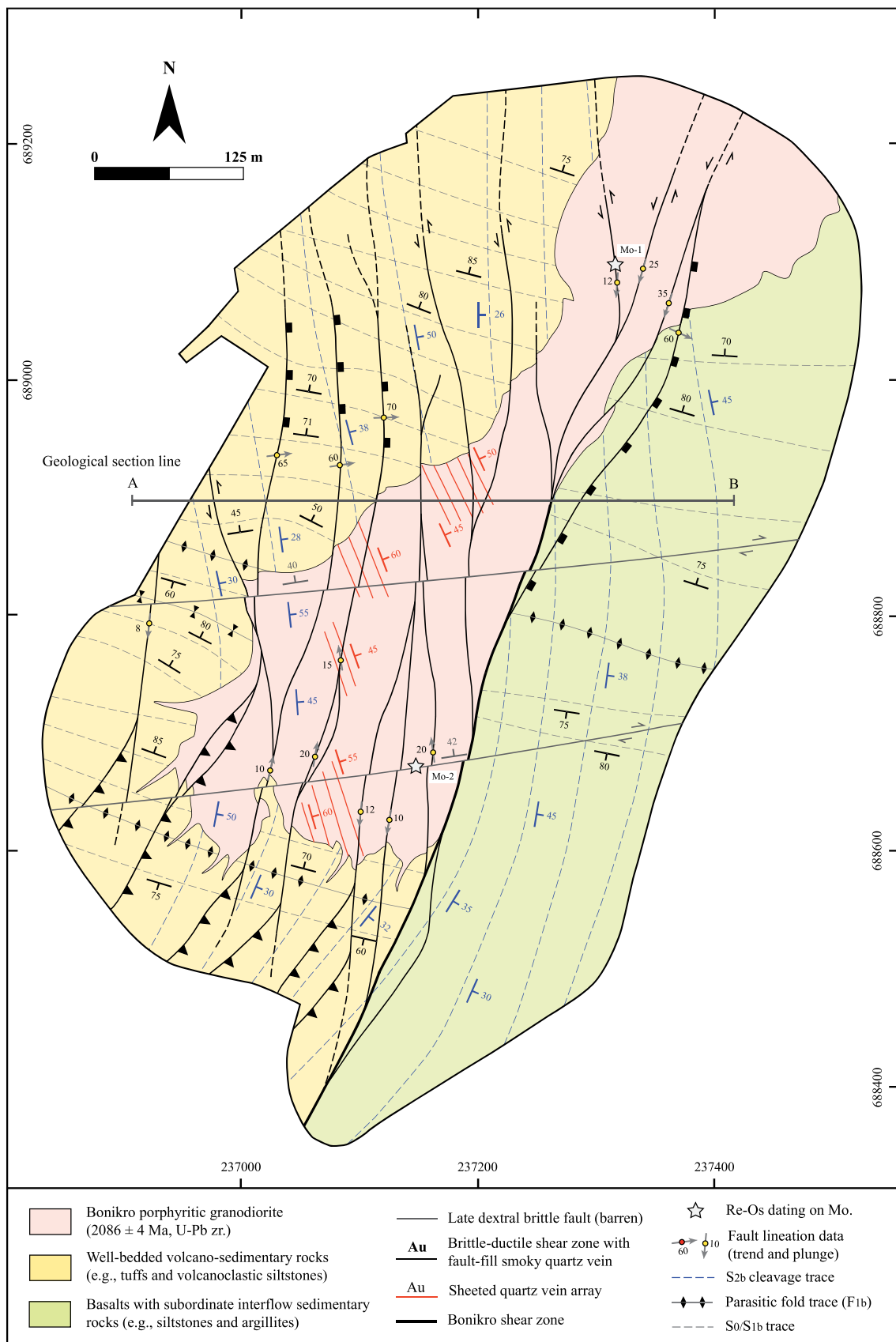
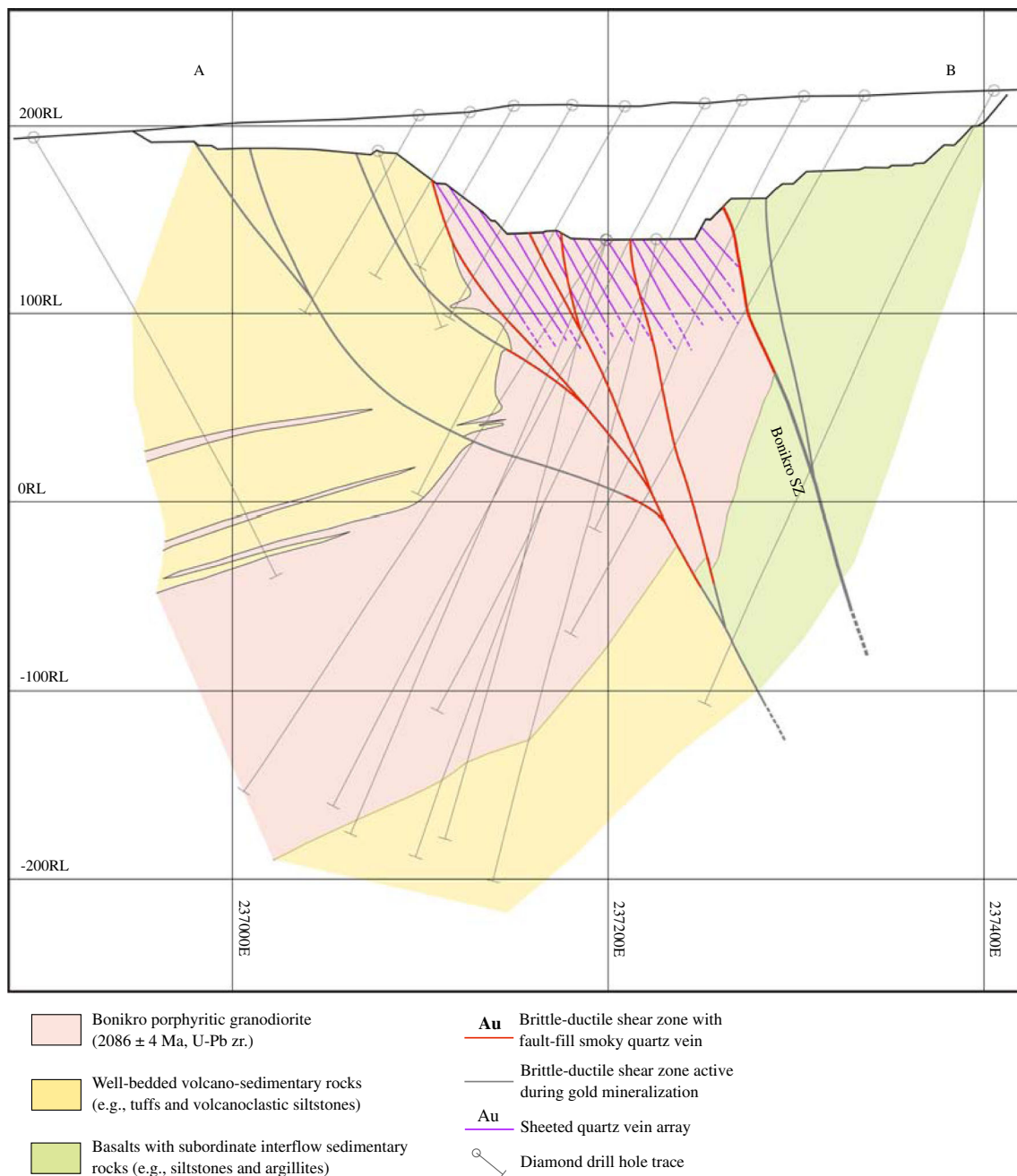**Fig. 3** Geological map of the Bonikro open pit

Fig. 4 Representative geological section through the central part of the Bonikro deposit. Section line located in Fig. 3

brown to greenish biotite, epidote, actinolite and trace amounts of albitic plagioclase that locally enclose the remains of clinopyroxene and hornblende phenocrysts. Metamorphosed sedimentary rocks west of the porphyritic granodiorite now comprise intergrown green–brown biotite, epidote, actinolite, chlorite, minor sericite and trace albite, carbonate and quartz. No primary detrital grains remain. However, the mafic character of this metamorphic assemblage implies these sedimentary rocks have mafic siltstone and/or tuff protoliths. Mineral assemblages in rocks east and west of the granodiorite porphyry are typical of the mid to upper greenschist-facies and comparable with those in the Toumodi Group throughout the Bonikro area.

Margins of the Bonikro pluton intrude the adjacent volcanic and volcano-sedimentary rocks with numerous rafts and xenoliths of the country rocks locally present in more gently dipping parts of the granodiorite cupola. Dykes of K-feldspar-rich pegmatite and aplite that locally contain minor biotite and tourmaline cut the carapace of the pluton and adjacent volcanic and volcano-sedimentary rocks. A 1–2-m-wide contact-metamorphic aureole that includes deep red to brown biotite, hornblende, pyrite (≤3%) and magnetite (≤1%) partially encloses the southwestern part of the granodiorite porphyry.

Bedding on either side of the Bonikro granodiorite porphyry strikes WNW–ESE, implying the distinct lithological units

on either side of the intrusive body were juxtaposed at sharp contact across a shear zone (Figs. 3 and 4). This shear zone is preserved in the southern part of Bonikro open pit, south of the pluton. Although aligned phenocrysts locally define a magmatic fabric within the granodiorite, post-emplacement reactivation of this shear zone has resulted in local intracrystalline deformation of the pluton.

Plutonic host rocks at Hiré

The Hiré gold deposits are located within the Kan River Plutonic Complex. The Chapelle and Akissi-So plutons comprise metaluminous plagioclase-phyric, biotite- and hornblende-bearing tonalite and granodiorite and, thus, are interpreted to belong to the Diéri-Kouassikro suite (Fig. 2). Accessory minerals include titanite, apatite, zircon and allanite. These plutons locally contain mafic xenoliths. Least-altered specimens are generally only weakly deformed, but zones of intense solid-state deformation occur within shear zones that cut the Chapelle and Akissi-So plutons and their alteration envelopes.

Bonikro deformation history and structural architecture

Four phases of deformation are recognised at Bonikro, here denoted D_{1b} through D_{4b}. Bedding throughout the Bonikro open pit strikes WNW and dips moderately to steeply either towards the NNE or SSW (Fig. 3 and 5a), discordant to the regional NNE-striking structural grain, suggesting Bonikro is located on the limb of an upright, steeply plunging, WNW-striking F_{1b} fold. Changes in the dip direction of bedding imply the presence of numerous parasitic F_{1b} folds. Bedding is locally partly transposed into the axial–planar cleavage (S_{1b}). Bedding orientations and the F_{1b} fold geometry are consistent with N to NNE shortening during D_{1b}.

The Bonikro Shear Zone juxtaposed lithologically distinct rock packages on either side of the Bonikro pit during D_{2b}, with displacement on the shear zone spanning emplacement of the Bonikro granodiorite porphyry. The penetrative NNE-striking, gently to moderately ESE-dipping S_{2b} cleavage and parallel second-order D_{2b} thrust faults, related to the Bonikro Shear Zone, cut bedding and the aforementioned F_{1b} folds in volcanic and volcano-sedimentary rocks on either side of the Bonikro pluton (Fig. 3). The main Bonikro porphyritic granodiorite cuts across S_{2b}, indicating the main pluton was emplaced relatively late in D_{2b}. However, some porphyritic granodiorite dykes on the margin of the main pluton, in the northern part of Bonikro open pit, were emplaced subparallel to S_{2b} and then deformed by S_{2b}. Furthermore, some pegmatite dykes were also affected by F_{2b} folds. The contractional character of D_{2b} is reflected in the steep amphibole stretching lineation commonly observed on S_{2b} fault planes in meta-basalts (Fig. 5b) and up-dip stepped calcite fibres on some S_{2b} planes that indicate reverse displacement (Fig. 5c). Further relict up-dip stepped mineral fibres are present within parts of the Bonikro Shear Zone that were less intensely reworked after emplacement of the main Bonikro pluton. Quartz–calcite veins, 1–30 cm wide, formed synchronous with the S_{2b} cleavage and were boudinaged during subsequent deformation. Fold and shear zone geometry and kinematic indicators together indicate WNW–ESE shortening during D_{2b}.

A sheeted quartz vein array that crosscuts S_{2b} developed almost exclusively within the cupola of the Bonikro porphyritic granodiorite during the early part of D_{3b} (Figs. 3 and 4). Closely spaced 0.2–1 cm thick veins within this array (Fig. 6a, b) are typically oriented N 340–350°/45–65° E. In the central part of the open pit, these sheeted quartz veins are cut by a swarm of N- to NNE-striking brittle faults that dip 50–85° E and which formed during the latter part of D_{3b} (Figs. 3 and 7a, b). These faults locally host smoky grey quartz–molybdenite veins up to a metre thick (Fig. 7c, d). They are confined to the porphyritic granodiorite and merge with the Bonikro shear zone in the southern part of the open pit. Narrower, gently dipping (30–50°), NE-striking horsetail faults that cut the volcano-sedimentary rocks in the southern end of the open pit splay off the more steeply dipping extensive faults in the central part of the pit (see Fig. 3). Fault planes are commonly coated with molybdenite and locally minor pyrite. Two sets of slickenlines and associated stepped fibres on the steeply dipping N-striking fault planes indicate sinistral–(normal) and normal displacement, respectively, during the latter part of D_{3b}. The attitude of S_{2b} locally changes to a N–S strike and steeper dip within D_{3b} fault corridors due to kink folds, fault drag and anticlockwise rotation. Fault and vein geometry and lineation data are consistent with a local transtension zone under region-wide NW–SE-directed shortening during D_{3b}.

A late generation of ENE-striking brittle faults, that dip moderately to the north, crosscut all D_{1b}–D_{3b} structures during D_{4b} (Fig. 3). These faults are 0.1–1 m wide and occur as parallel sets. Whereas milky white quartz veins are locally developed along the D_{4b} faults, the fault surfaces are commonly coated with molybdenite. Molybdenite slickenlines and associated stepped fibres indicate dextral displacement on the faults. Fault geometry and lineation data are consistent with E–W-directed shortening during D_{4b}.

Hiré deformation history and structural architecture

A moderate to strong, WNW- to NW-striking, gently SW-dipping penetrative planar fabric (S_{1h}) is the earliest structure observed at Chapelle (Fig. 8). Metre-wide zones of stronger S_{1h} foliation development include en-échelon quartz veins

Fig. 5 **a** Well-bedded meta-volcanoclastic siltstones and meta-tuffs in the western part of the open pit. Bedding measurements consistently strike WNW–ESE, which is at the right angle to the region-wide NNE–SSW-striking structural grain. **b** Steep amphibole stretching lineation on S_{2b} planes in meta-basalts. **c** Up-dip calcite stepped fibres on S_{2b} planes in meta-basalts indicate thrusting towards the west. Insets show structural data plotted in equal area stereonets, lower hemisphere projection
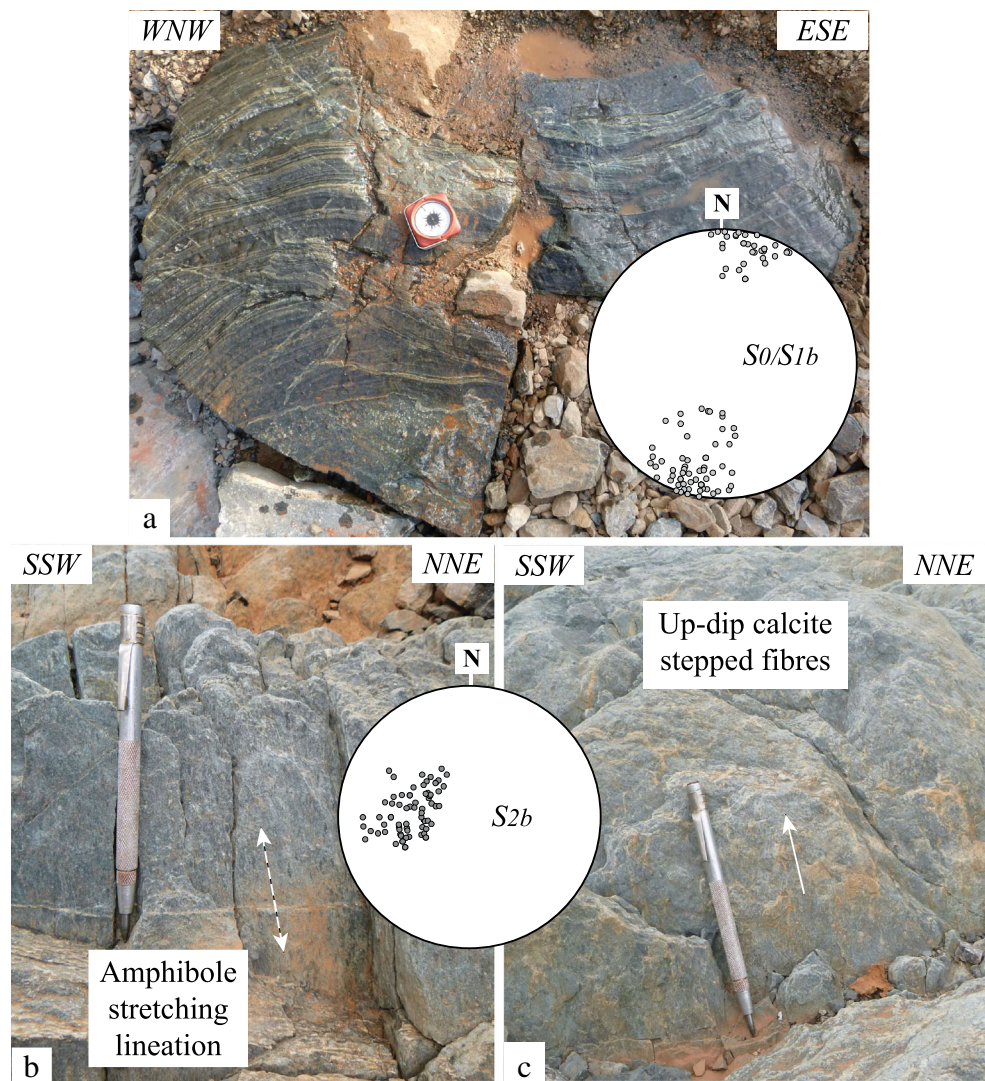
whose asymmetry and attitude imply they formed during reverse displacement on S_{1h} (Figs. 8 and 9a). Primary interstitial quartz within these more strongly deformed zones forms elongate recrystallised lenses enclosed by S_{1h} folia, whereas plagioclase phenocrysts, more resistant to deformation, are rotated towards parallelism with S_{1h}. Micaceous S_{1h} folia also enwrap dismembered micro-lenses of the plutonic rock. The orientation of S_{1h} and geometric relationships between S_{1h} and the en-échelon veins indicate NNE–SSW-directed shortening during D_{1h} at Chapelle.

A moderate to strong, N- to NNE-striking and gently W- to NW-dipping S_{2h} foliation at Chapelle and Akissi-So is developed in an array of NE-striking, moderately NW-dipping shear zones. Slickenlines and S-C fabrics indicate reverse displacement towards the SE during WNW–ESE-directed shortening D_{2h} at Hiré.

ENE-striking, steeply SSE-dipping D_{3h} brittle-ductile shear zones that are 1–5 m wide cut across D_{1h} and D_{2h} structures at Chapelle (Fig. 8). D_{3h} shear zones are marked by pervasive, texturally destructive, reddish alteration and locally contain 2–10 cm wide smoky quartz veins (Fig. 9b, c). At Chapelle, S-C fabrics and stepped slickenline fibres indicate dextral displacement on these shear zones during D_{3h}. Similar ENE- to NE-striking but steeply NW-dipping rather than SE-dipping D_{3h} brittle-ductile shear zones cut D_{1h} and D_{2h} structures at Akissi-So. There, S-C fabrics and stepped slickenline fibres indicate reverse to sinistral-reverse displacement on the NE-striking D_{3h} shear zones and dextral displacement along the ENE-trending D_{3h} shear zones. Although local variations of the far-field stress are to be expected within a large heterogeneous plutonic complex, shear zone geometry, associated tension quartz veins and kinematic indicators at both Chapelle and Akissi-So are consistent with WNW–ESE- to NW–SE-directed shortening D_{3h}.

Late barren brittle D_{4h} faults that comprise chloritic granitoid cataclasite and gouge cut D_{1h}–D_{3h} structures. Correlation

Fig. 6 **a** Typical field view of the sheeted quartz vein array in the Bonikro granodiorite porphyry. These sheeted quartz veins show little to no variation in strike and dip. Inset shows structural data plotted in an equal area stereonet, lower hemisphere projection. **b** Representative diamond drill core intersect of the sheeted quartz vein array
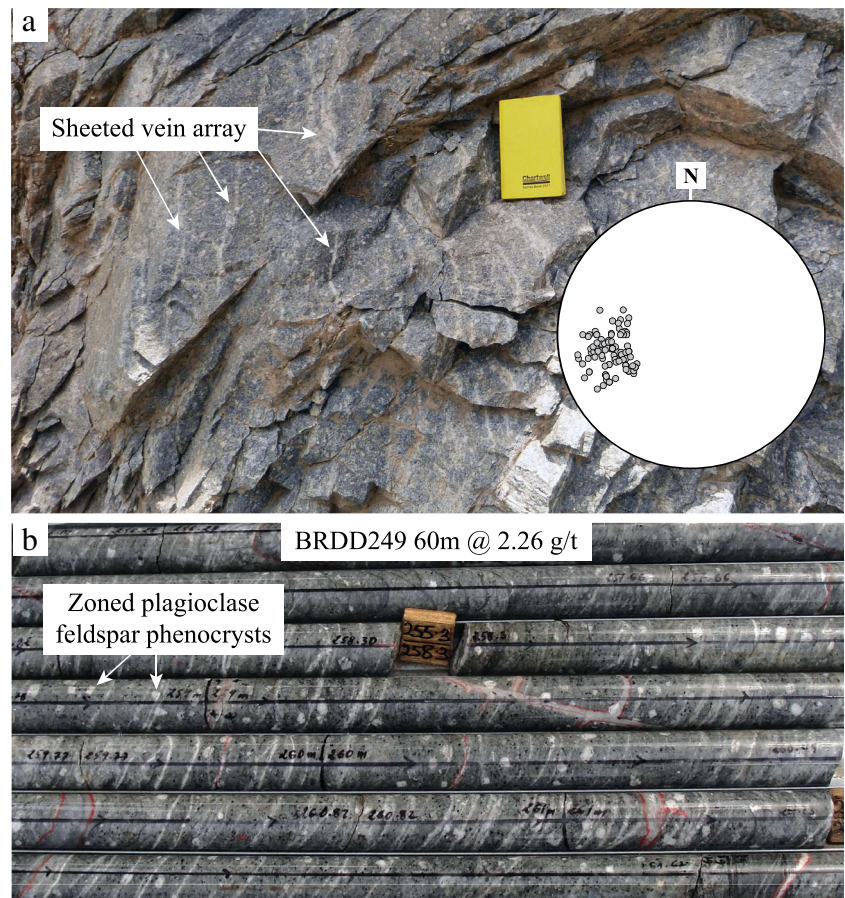
Bonikro ore and alteration paragenesis

Four generations of quartz veins are present at Bonikro: (1) barren quartz–carbonate veins parallel to S_{2b}, (2) auriferous sheeted quartz vein arrays, (3) auriferous fault-fill smoky quartz-molybdenite veins and (4) late fault-fill barren quartz-molybdenite veins. The two generations of auriferous quartz veins developed during D_{3b}.

The early barren veins parallel to S_{2b} comprise quartz and carbonate, with more than 90% quartz where they cut volcano-sedimentary rocks and up to 40% carbonate where they cut meta-basaltic rocks. These early veins are not associated with obvious alteration haloes in the surrounding rocks.

Arrays of sheeted quartz veins, typically 15–50 m wide, host low- to medium-grade (~0.5–2 g/t) gold mineralisation. Increases in vein density correlate with increases in gold grade. Sheeted veins are almost exclusively developed in the main pluton of porphyritic granodiorite. They consist of quartz (>80%), calcite (up to 10%), albite (up to 10%) and traces of pyrite (up to 1%). Quartz within the sheeted veins is commonly recrystallised, having been deformed during

incremental deformation in the latter stages of D_{3b}. Calcite, albite and pyrite are generally concentrated on vein margins. The sheeted quartz veins are associated with beige to greenish haloes of wall rock alteration up to 2 cm wide that include albite ± sericite, calcite, biotite, pyrite, ilmenite, rutile, native gold, scheelite and Bi–Pb–tellurides. Primary plagioclase is replaced by albite, whereas wispy sericite-rich laminae anastomose around variably strained and altered phenocrysts and define a spaced, planar fabric subparallel to the veins. Fine-grained calcite and lesser amounts of brown biotite infill microfractures in the altered porphyry groundmass. Primary igneous biotite is replaced by fine-grained sericite. Ilmenite and traces of rutile and magnetite pseudomorph primary titanite. Pyrite is the dominant sulfide, and generally euhedral, but locally occurs as elongated crystals within S_{2b}. A wide range of accessory minerals are also present in vein and alteration haloes, including pyrrhotite, scheelite, molybdenite, galena, tellurobismuthite, tetradymite (Bi_2Te_2S), rucklidgeite (($Bi,Pb)_3Te_4$), altaïte ($PbTe$), kochkarite ($PbBi_4Te_7$) and volynskite ($AgBiTe_2$) (Fig. 10a, b). Native gold that contains 5–20% Ag occurs in the altered wall rocks around the sheeted veins as (i) inclusions in pyrite (~2–16 μm), (ii) native gold particles closely associated with pyrite (up to 35 μm) and (iii) blebs of native gold (~1–6 μm) along microfissures in pyrite

Fig. 7 a Fault swarm and associated fault-fill smoky quartz veins dissecting the Bonikro porphyritic granodiorite in the central part of the open pit. Insets show structural data plotted in an equal area stereonet, lower hemisphere projection. b Cross-cutting relationship between the fault-fill smoky quartz veins and earlier sheeted quartz veins. c Fault-fill smoky quartz vein containing molybdenite lamina, potentially indicating multiple episodes of shearing. d Representative diamond drill core intersect of the fault-fill smoky quartz veins
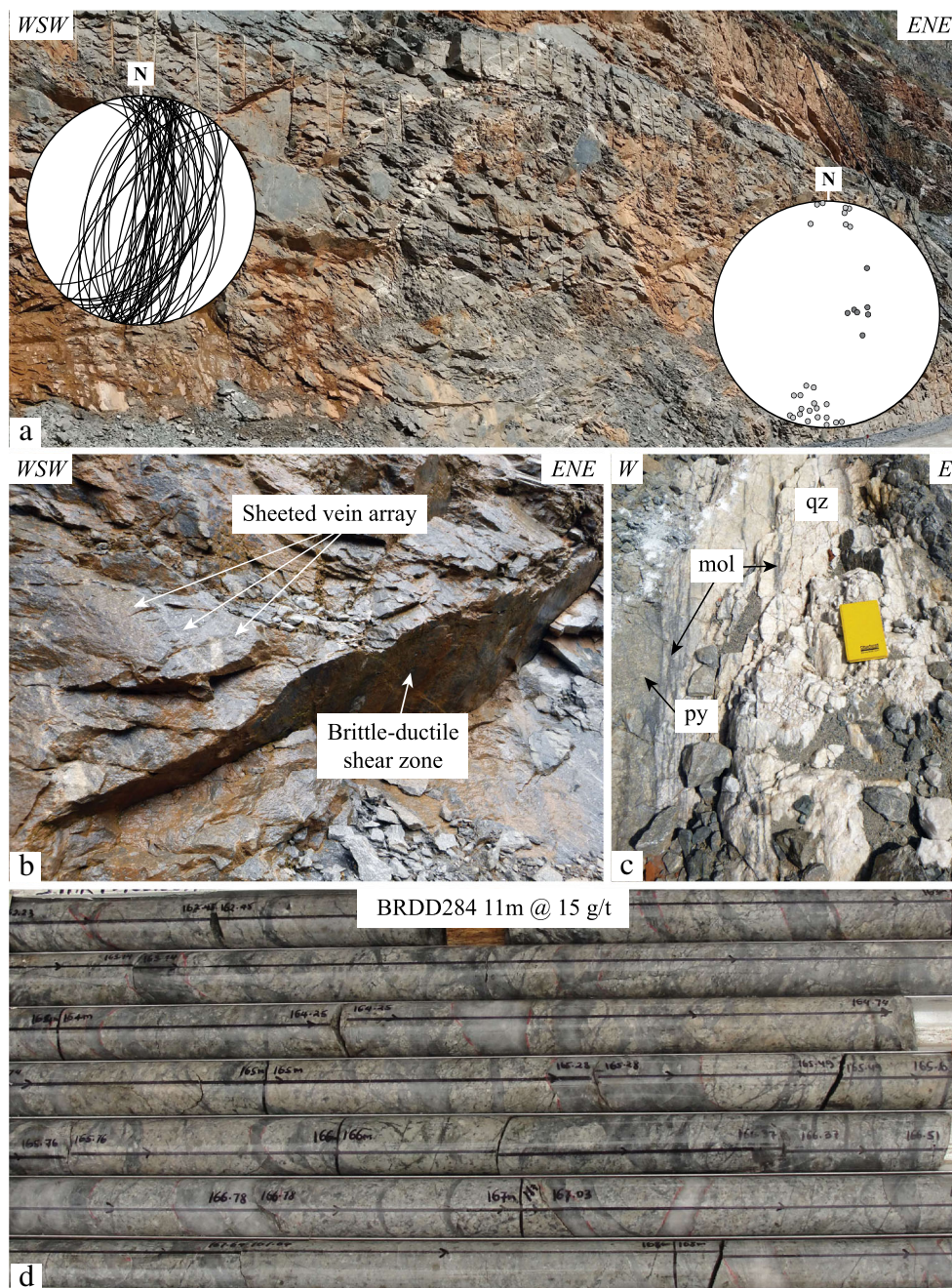
(Fig. 10c, d). Visible gold has also been observed in rare occasions in the sheeted veins rather than altered wall rocks.

The fault-fill smoky quartz–molybdenite veins are associated with 2–10 m wide zones of higher-grade (> 3 g/t) gold mineralisation. Individual smoky quartz–molybdenite veins consist of quartz (> 90%), calcite and/or Fe-dolomite (up to 5%), molybdenite (up to 4%), pyrite (up to 1%) and gold. Molybdenite is concentrated along the vein margins and in coatings on associated slickenlined fault planes. Native gold within the smoky quartz veins occurs as fine-grained specks up to 1 mm in size. Quartz within the veins is recrystallised, exhibiting features such as undulose extinction, bulging and/or subgrain rotation. Smoky quartz–molybdenite veins are associated with haloes of sericite + albite ± calcite and/or Fe-dolomite, chlorite, pyrite, rutile, native gold and molybdenite alteration. Pyrite, the dominant sulfide species, is commonly intergrown with fibrous molybdenite (Fig. 10e). Traces of pyrrhotite, chalcopyrite, galena, tetradymite, kochkarite, volynskite and wolframite are also present in the veins and their alteration haloes (Fig. 10e, f). Native gold in the altered wall rocks contains 1–20% Ag and forms, in order of decreasing abundance: (i) native gold inclusions in pyrite and molybdenite (~ 2–20 μm), (ii) native gold particles closely associated with pyrite (up to 50 μm) and (iii) native gold blebs (~ 1–
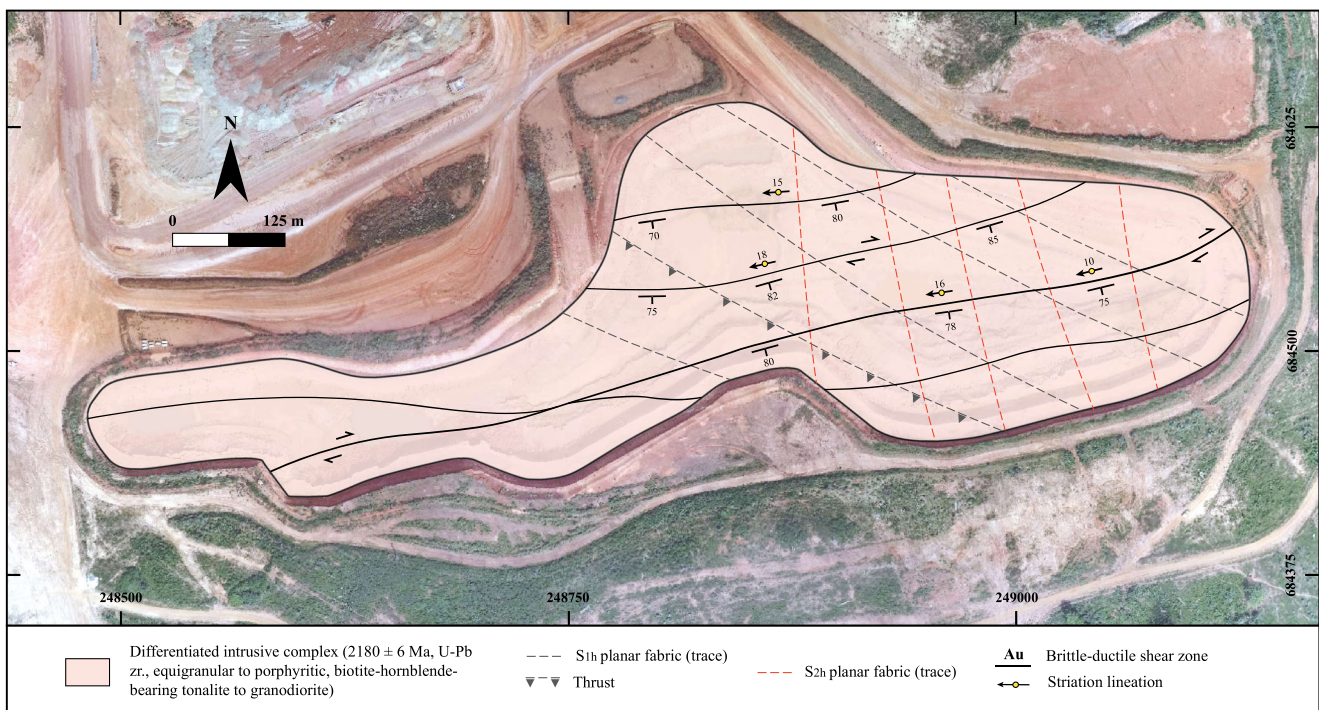
Fig. 8 Geological map of the Chapelle open pit

5 μm) in microfissures that cut pyrite (Fig. 10f–h). Geological sampling and assaying indicates the late, D_{4b} fault-fill quartz-molybdenite veins are barren. They consist of white quartz (> 90%), molybdenite (≤ 10%) and traces of pyrite (up to 1%).

Hiré ore and alteration paragenesis

At Chapelle, zones of D_{1h} protomylonite to mylonite and S_{1h} development are associated with sericite + chlorite + albite ± quartz, biotite, calcite, zoisite, epidote, pyrite, magnetite and rutile alteration. Igneous plagioclase grains near the margins of these zones are largely replaced by albite + sericite ± chlorite, zoisite and biotite, whereas grains near the centre of these altered zones are replaced albite and very-fine-grained sericite. Accompanying biotite and hornblende are altered to sericite + chlorite ± zoisite and calcite, whereas rutile pseudomorphs igneous titanite. Magnetite is intergrown with pyrite along S_{1h}.

The texturally destructive reddish alteration in the mineralised D_{3h} shear zones includes abundant calcite + lesser chlorite + albite ± sericite, biotite, pyrite, magnetite, hematite, rutile and native gold. Within the D_{3h} shear zones, plagioclase is partially to completely replaced by albite and very-fine-grained sericite. Twin lamellae within hydrothermal albite are kinked and cut by chlorite–calcite microshears indicating alteration was synchronous with on-going D_{3h} deformation. Ragged patches of intergrown calcite and chlorite commonly replace earlier microfractures, or form chlorite–calcite–pyrite–magnetite veins with thin albite–chlorite–calcite–sericite–

pyrite–magnetite–hematite-altered selvages. Variably oriented pyrite veins, 1–5 cm wide, also occur within the altered D_{3h} shear zones. The reddish colour of these sheared and mineralised rocks reflects the presence of fine-grained hematite as (i) discrete blades intergrown with clusters of chlorite and calcite grains, (ii) submicron specks dusting plagioclase and (iii) replacement of patches within magnetite grains. Pyrite is the dominant sulfide, comprising up to 2% of the altered rocks in the D_{3h} shear zones. Magnetite and pyrite are intergrown and have euhedral crystal shapes (Fig. 11a). Locally pyrite crystals are rimmed by chlorite. Native gold that contains 1–14% Ag occurs as, in decreasing abundance, (i) inclusions ~ 1–6 μm across in pyrite, (ii) free gold particles up to 250 μm across closely associated with pyrite and/or magnetite and (iii) (~ 1–5-μm-sized blebs) filling microfissures in pyrite (Fig. 11a, b).

At Akissi-So, zones of S_{2h} development are associated with sericite + chlorite + albite ± quartz ± biotite ± calcite ± zoisite-epidote ± pyrite alteration, similar to the alteration that characterises the S_{1h} shear zones at Chapelle. However, the texturally destructive alteration that overprints the mineralised D_{3h} shear zones at Akissi-So is distinct from that at Chapelle and includes sericite + quartz + Fe-dolomite ± albite and pyrite. Ragged patches and fine-grained flecks of sericite define the S_{3h} shear fabric. Associated D_{3h} shear veins consist of quartz with minor Fe-dolomite, chlorite and pyrite, whereas the adjacent wall rock alteration haloes include proximal sericite + Fe-dolomite + pyrite + rutile and distal chlorite + calcite ± zoisite–epidote assemblages. Plagioclase is partly to

Fig. 9 **a** En-échelon sigmoidal quartz tension veins marking a thrust zone in the Chapelle open pit. **b**, **c** Array of steep ENE-striking brittle-ductile shear zones and associated fault-fill quartz veins in the Chapelle (**b**) and Akissi-So (**c**) open pits, respectively. Insets show structural data plotted in equal area stereonets, lower hemisphere projection
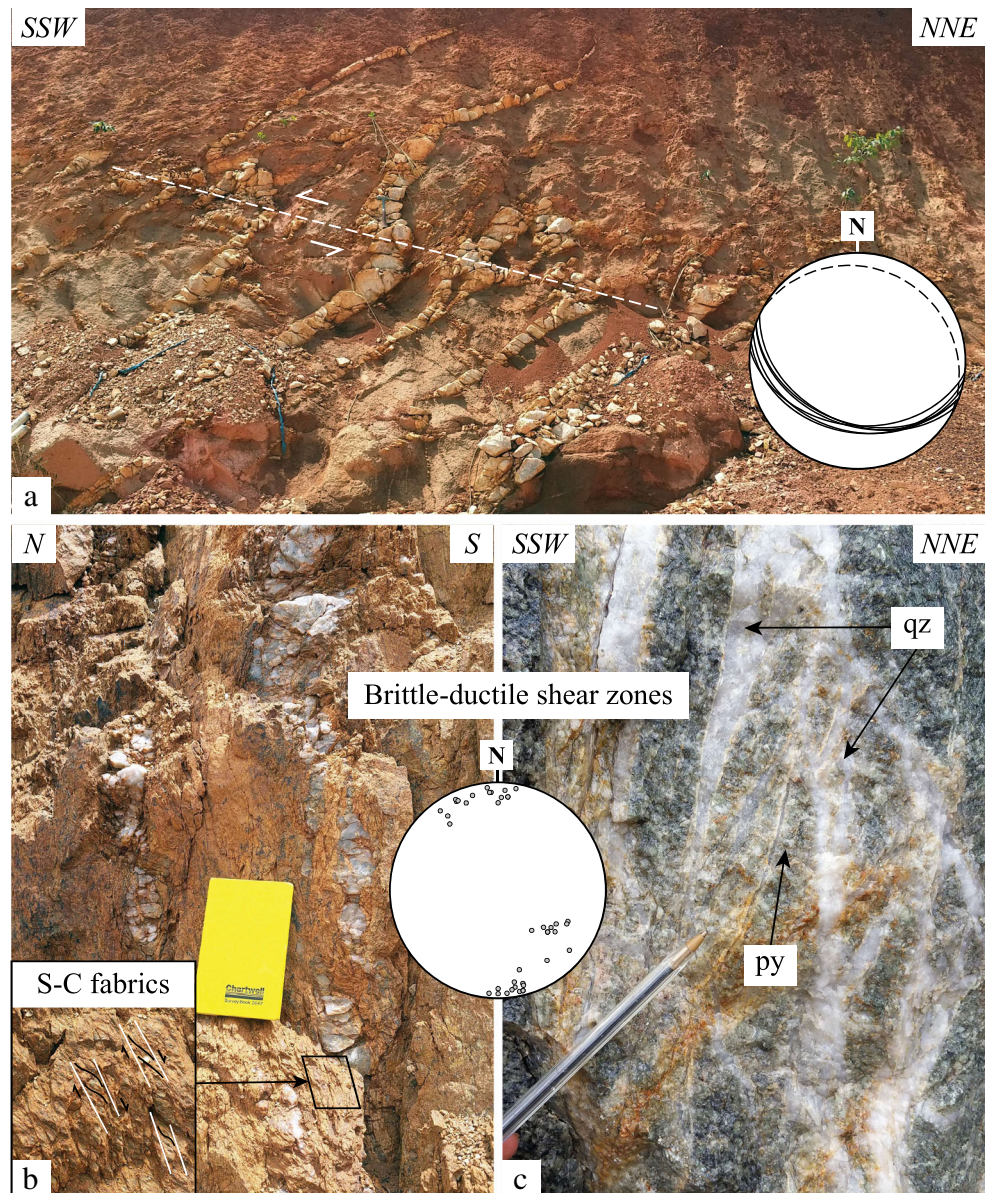
completely replaced by albite and fine-grained sericite, whereas biotite and hornblende are replaced by chlorite, calcite, zoisite and epidote, and titanite by rutile. Pyrite is the dominant sulfide and commonly occurs with traces of magnetite. Native gold that contains 1–12% Ag occurs as ~ 1–5 μm inclusions in pyrite.

Timing of magmatic and hydrothermal events

The Bonikro porphyritic granodiorite contains a uniform population of translucent, colourless, euhedral zircon grains 80 to 200 μm long with sharp terminations and fine oscillatory zoning (Fig. 12a, b). The grains contain 60–500 ppm Th and 110–320 ppm U and have Th/U ratios between 0.44 and 1.53, with most values below < 1,

consistent with a magmatic origin (Williams et al. 1996; Wang et al. 2011; Kirkland et al. 2015). Nineteen analyses were performed on 17 zircons with 18 out of 19 analyses within ± 5% of the Concordia (Table 1). All zircon analyses define a discordia line with upper and lower intercepts of 2086 ± 4 Ma (MSWD = 0.6) and − 88 ± 150 Ma, respectively. The lower intercept is zero within error and allows calculation of a ^{207}Pb/^{206}Pb weighted mean age for the 18 concordant analyses of 2087 ± 5 Ma (MSWD = 0.5) (Fig. 12c). The 2086 ± 4 Ma U–Pb zircon age is interpreted as the crystallisation age of the Bonikro porphyritic granodiorite.

The Chapelle granodiorite contains a uniform population of colourless to light brown, subhedral to euhedral zircon grains up to 250 μm long with sharp terminations and fine

Fig. 10 **a**, **b** BSE photomicrographs showing the representative ore assemblage associated with the sheeted quartz veins. **c**, **d** Photomicrographs illustrating gold deportment in sheeted quartz veins and wall rocks. **e**, **f** Photomicrographs showing the representative ore assemblage associated with the fault-fill smoky quartz veins. Note that gold-bearing pyrite (as native gold inclusions) is intergrown with molybdenite. **g**, **h** Photomicrographs illustrating gold deportment in the fault-fill quartz veins and wall rocks. sch—scheelite, mol—molybdenite, gn—galena, ttd—tetradymite, rck—rucklidgeite, tlb—tellurobismuthite, kok—kochkarite, vsk—volynskite
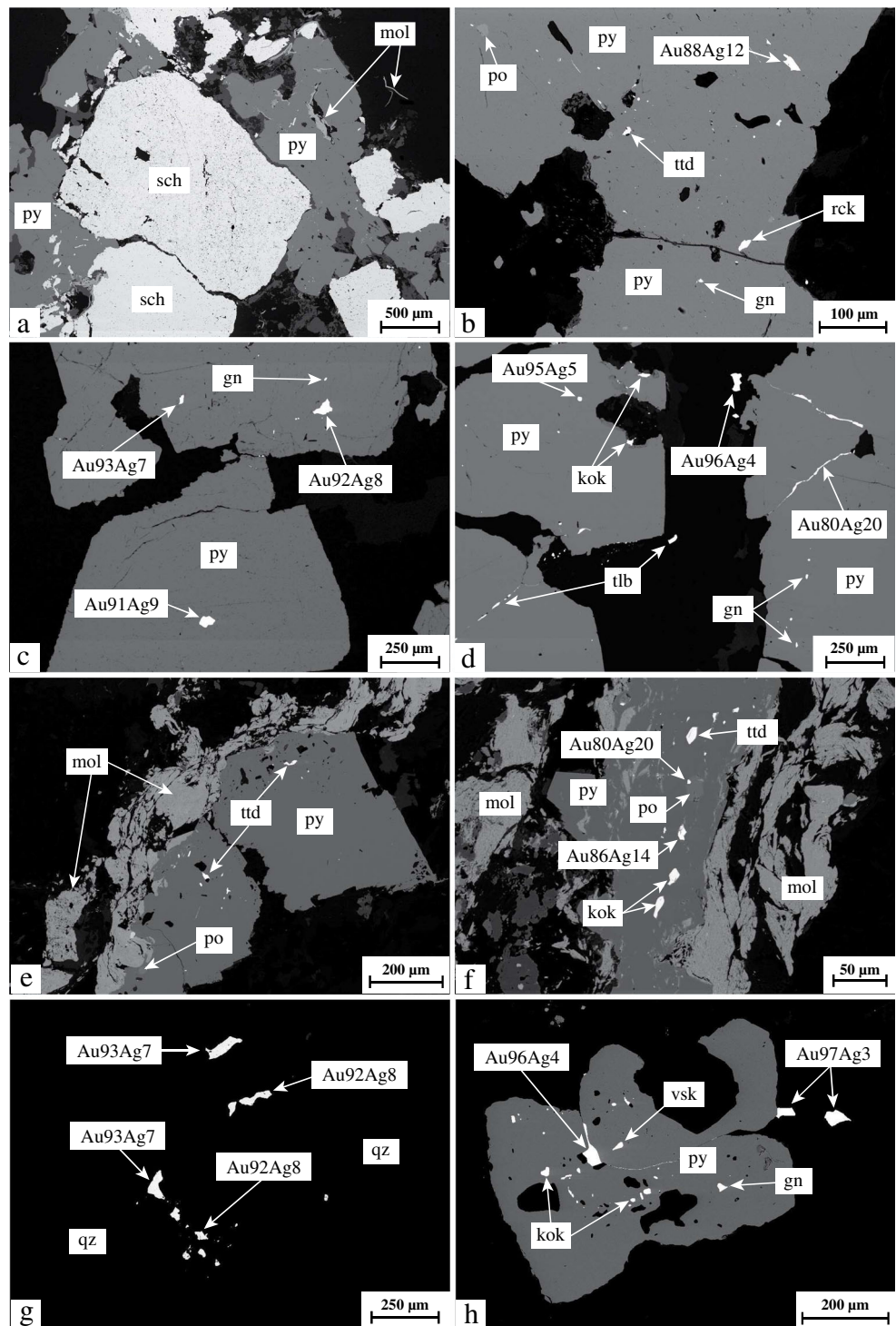
oscillatory zoning (Fig. 12d). Twenty-two analyses were performed on 22 zircons. Eleven of the 22 zircon analyses are > 5% discordant (Table 1), and these analyses were not included in the calculated age of the sample. One near-concordant analysis has a $^{206}Pb*/^{238}U*$ age of 2219 ± 16 Ma and is interpreted as an inherited grain. The ten remaining zircons define a discordia line with upper and lower intercepts of 2179 ± 11 Ma (MSWD = 2.6) and − 363 ± 400 Ma, respectively.

The lower intercept is zero within error and allows calculation of a $^{207}Pb/^{206}Pb$ weighted mean age of 2180 ± 6 Ma (MSWD = 1.12) for the ten near-concordant grains (Fig. 12e), which is interpreted as the crystallisation age of the Chapelle granodiorite.

Sample Mo-1, from a steep N-striking fault-fill quartz vein that cuts the Bonikro porphyritic granodiorite, consists of smoky quartz with 1–2% molybdenite along the vein

Fig. 11 a The ore assemblage is dominated by pyrite with minor to traces of magnetite. Pyrite and magnetite occur intergrown (reflected light). **b** BSE photomicrograph illustrating gold deportment within the brittle-ductile shear zones
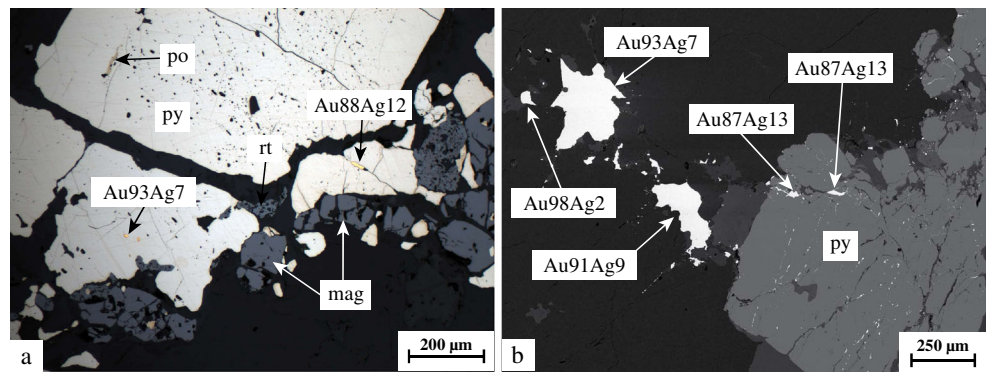
boundaries and disseminated pyrite in the adjacent pluton. The 2074 ± 16-Ma Re–Os age of the molybdenite in this vein is interpreted as the timing of higher-grade gold mineralisation late in D_{3b} at Bonikro (Table 2).

Sample Mo-2 is from a late barren D_{4b} fault in the central part of Bonikro open pit. The slip plane of the fault is coated with molybdenite. The 2041 ± 18-Ma Re–Os age of this molybdenite is interpreted as the minimum age for gold

Fig. 12 a, **b** BSE photomicrographs illustrating zircon morphology from the Bonikro porphyritic granodiorite. Note the sharp terminations and fine oscillatory zoning, which reflect a magmatic origin. **c** U–Pb Concordia plot for zircon analyses from the Bonikro porphyritic granodiorite. **d** Photomicrograph illustrating zircon morphology from the Chapelle granodiorite. **e** U–Pb Concordia plot for zircon analyses from the Chapelle granodiorite
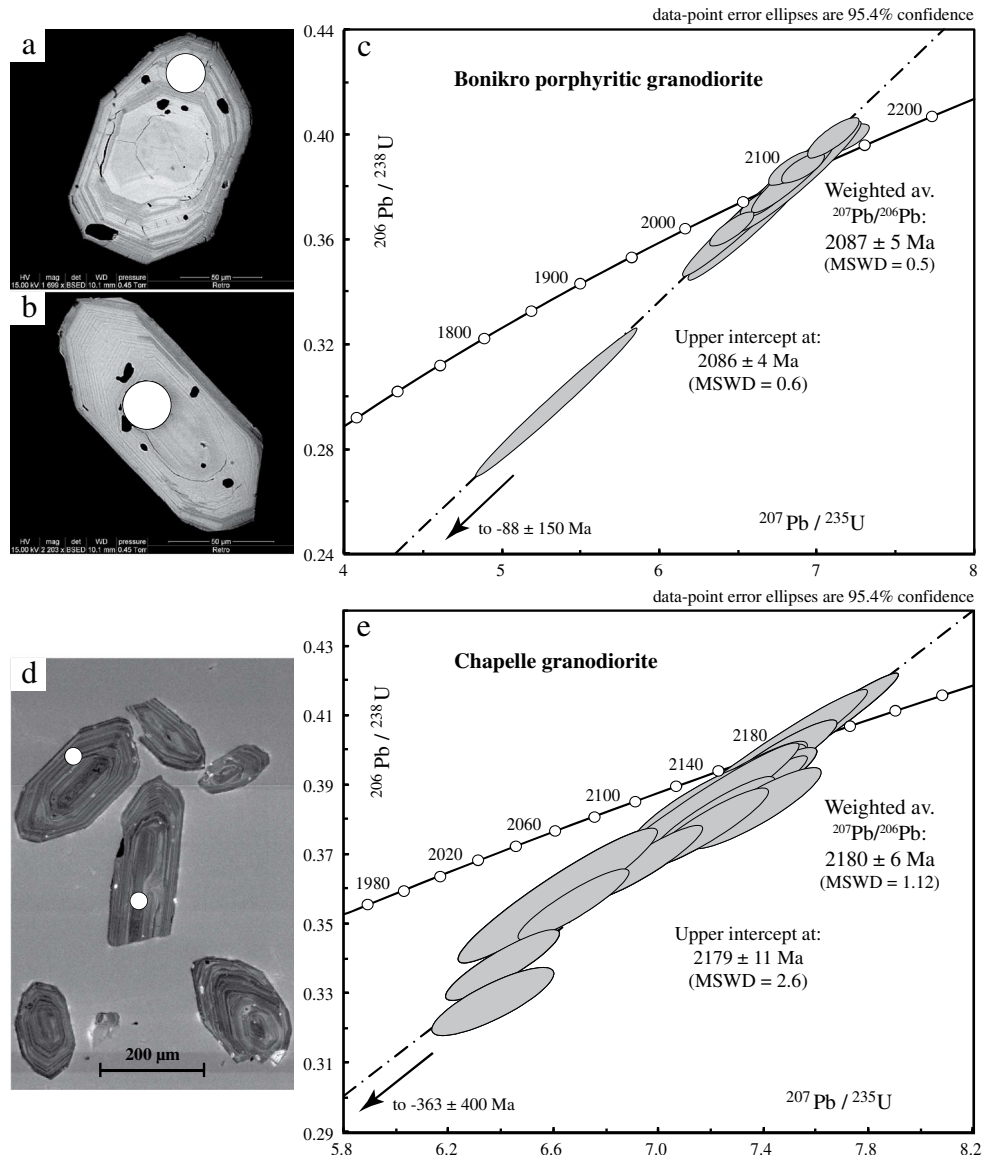
Table 2 Re–Os data obtained on molybdenite from the Bonikro gold deposit

ID	Mineral phase	Sample mass (g)	[Re] (ppb)	^{187}Re (ppb)[1] $\pm 2\sigma$	Total ^{188}Os (ppb)[2]	Total ^{187}Os (ppb)	%^{187}Os*[3]	^{187}Os* (ppb)[1, 3] $\pm 2\sigma$	^{187}Os*/^{187}Re[1, 3] $\pm 2\sigma$	Age (Ma)[1, 4] $\pm 2\sigma$
Mo-1	Mo	0.09956	12,149	7638 ± 52	0.017	268.4	100.0	268.4 ± 0.2	0.0351 ± 0.0003	2074 ± 16
Mo-2	Mo	0.12858	18,457	11,603 ± 90	0.012	401.3	100.0	401.3 ± 0.3	0.0370 ± 0.0003	2041 ± 18

[1] All listed uncertainties are 2σ

[2] Includes both common osmium contained in the sample and the contribution from the blank

[3] ^{187}Os* = ^{187}Os radiogenic only, calculated assuming a natural osmium ratio of ^{187}Os/^{188}Os = 0.5 ± 0.4. Uncertainty on ^{187}Os* includes the uncertainty on this ratio, measurement precision, uncertainty on spike calibration and uncertainty on standard measurements

[4] Assuming $\lambda 187$Re = 1.666×10^{-11} year^{-1} (Smoliar et al. 1996)

mineralisation and the age of D_{4b} at Bonikro (Table 2). Some caution is needed when interpreting these single analysis Re–Os ages as they are derived from only two samples, but the ages are compatible with the field relationships.

Discussion

Integration with regional tectonics

An early episode of N–S-directed shortening, similar to that referred to as D_1 at Bonikro and Hiré, has been reported widely across Ghana (Perrouty et al. 2012; McFarlane 2018) and Burkina Faso (Hein 2010). Recognition of early NNE–SSW-directed shortening at Bonikro, Chapelle and Akissi-So suggests this event also affected south-central Côte d'Ivoire, after emplacement of the Chappelle granodiorite at 2180 ± 6 Ma, which is the best age estimate to date for the Diéri-Kouassikro suite within the Kan River Plutonic Complex.

The NNE-striking structural grain of the Oumé-Féttékro Belt, as defined by the strike of stratigraphic units, the Boni-Andokro Shear Zone, and the penetrative S_2 fabric, developed during D_2 WNW–ESE-directed shortening. This deformation episode has been recognised throughout the Baoulé-Mossi domain, including in eastern Côte d'Ivoire (Pouclet et al. 2006; Vidal et al. 2009), southwest Ghana where it was associated with inversion of the Kumasi Basin and folding of the Takwa Series (Allibone et al. 2002a; Perrouty et al. 2012; Feybesse et al. 2006), in Burkina Faso (Tshibubudze et al. 2009; Baratoux et al. 2011) and in southwestern Mali where it was associated with inversion of the Siguiri-Kofi Basin (Ledru et al. 1991; Lebrun et al. 2017; Masurel et al. 2017c). The orientation and sense of displacement on the Bonikro Shear Zone and NE-striking shear zones at Hiré imply that they developed during regional D_2, possibly as higher-order splays off the Boni-Andokro Shear Zone. Structural data collected in this study and the metamorphic break between greenschist-facies rocks of the Toumodi Group and higher-grade rocks of the Kan River Plutonic Complex suggest that the latter was thrusted over the Toumodi Group supracrustal

rocks during D_2, which contrasts with earlier interpretations by Mortimer (1990) and Leake (1992). The 2086 ± 4-Ma Bonikro porphyritic granodiorite likely emplaced late to post-D_2, ca. 100 Ma after crystallisation of intrusive rocks at Hiré.

One or more episodes of transcurrent/transpressional deformation, commonly referred to as D_3, are recognised throughout the Baoulé-Mossi domain between ca. 2100 and 2070 Ma (Liégeois et al. 1991; Milési et al. 1992; Feybesse et al. 2006; Pouclet et al. 2006; Vidal et al. 2009; Baratoux et al. 2011). The regional-scale sinistral Brobo shear zone, east of the Oumé-Féttékro Belt (see Fig. 2), is the principal D_3 structure in central Côte d'Ivoire (Mortimer 1990; Leake 1992). It truncates the D_2 Boni-Andokro shear zone and dissects the Oumé-Féttékro belt with up to 40 km of estimated left-lateral displacement (Mortimer 1990; Leake 1992). Kinematic data are compatible with D_{3b} and D_{3h} faults and fault-fill auriferous vein arrays at Bonikro and Hiré forming during this region-wide deformation episode. The switch from the D_2 pure shear-dominated compressional regime to simple shear-dominated tranpressional regime during D_3 has been linked to gold mineralisation across much of the Baoulé-Mossi domain (Goldfarb et al. 2017), and the Bonikro and satellite Hiré deposits appear to be another example of this.

Multistage ore deposition

Stage I gold mineralisation, restricted to Bonikro, comprises auriferous sheeted quartz veins within the uppermost part of the Bonikro porphyritic granodiorite (Fig. 13). This phase of gold mineralisation shares several characteristics with intrusion-related gold deposits, including (1) the relatively reduced, calc-alkaline to alkaline composition of the Bonikro granodiorite (Ouatarra 2015); (2) the presence of aplite and pegmatite dykes; (3) the sulfide-poor mineralogy of the sheeted veins; (4) the narrow 0.1–1-cm-wide alteration selvages around the sheeted veins implying a low fluid/rock ratio during vein formation; and (5) the Au ± Bi ± Te ± W ± Pb ± Mo metal association of the sheeted veins (Thomson and Newberry 2000; Lang and Baker 2001; Hart et al. 2002;
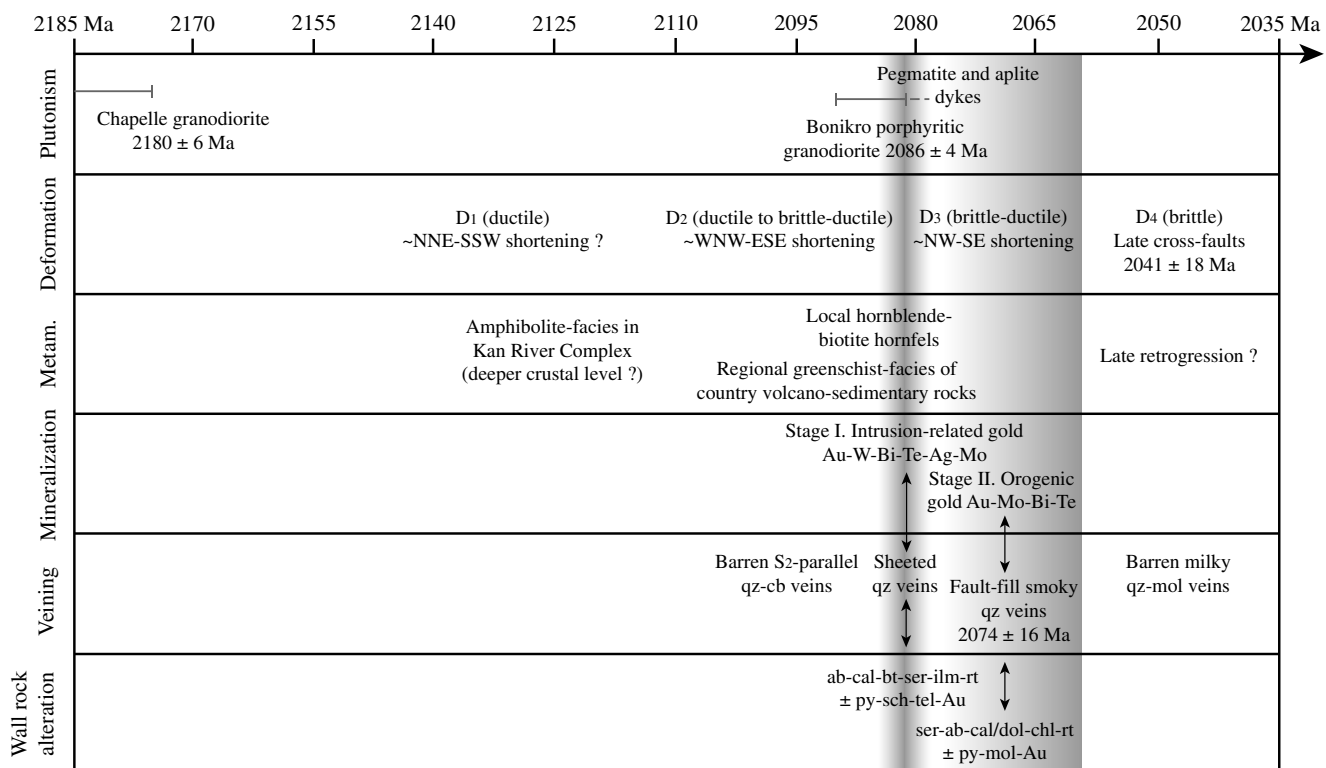
Fig. 13 Summary of the key timing and paragenetic relationships between magmatism, deformation, metamorphism and hydrothermal alteration at the Bonikro gold deposit

Hart 2005). The lack of miarolitic cavities within the Bonikro porphyritic granodiorite and the plutonic texture of its groundmass imply it was emplaced more than ~3 km below the paleosurface. The granodiorite was emplaced along the Bonikro shear zone as this structure was the main structural anisotropy in the surrounding rocks. Fractionation of a volatile-rich melt and the subsequent exsolution of a magmatic–hydrothermal fluid within the upper part of the Bonikro porphyritic granodiorite first produced the aplite and pegmatite dykes during the final stages of D_{2b} and then the mineralised sheeted quartz veins during the onset of D_{3b}. This model suggests that the change from compression during D_{2b} to transcurrent deformation during D_{3b} coincided with the final crystallisation of the Bonikro porphyritic granodiorite. Fracturing of the pluton carapace during strike-slip faulting may have been the critical event that extracted the auriferous magmatic–hydrothermal fluid from the carapace of the cooling pluton and focussed this fluid into the finely spaced sheeted fractures.

Stage II gold mineralisation, hosted by fault-fill auriferous quartz veins, formed within the plutonic rocks at Bonikro and Hiré during D_3 transcurrent faulting (Fig. 13). Textural evidence for solid-state deformation prior to this later phase of mineralisation at Bonikro is inconsistent with the porphyritic granodiorite acting as the source for fluids and metals. Relative and absolute geochronology indicate that the fault-fill auriferous, molybdenite-bearing vein, dated at 2074 ±

16 Ma, post-dated crystallisation of the porphyritic granodiorite and is interpreted as the timing of higher-grade gold mineralisation at Bonikro. At Chapelle and Akissi-So, no intrusion emplacement coincided with mineralisation, but the host rocks to both deposits were potentially emplaced ca. 100 Ma prior to mineralisation based on relative and absolute geochronology. The fault-fill character of the later mineralised veins at Bonikro and the auriferous veins at Chappelle and Akissi-So imply that the brittle rheology of the host granitoids, compared with the adjacent largely unmineralised supracrustal rocks, was the critical feature that focussed fluid flow. The structural setting, mineralogy and metal association of the altered and mineralised rocks at Chappelle and Akissi-So are typical of orogenic gold deposits, although the metal association of the later phase of mineralisation at Bonikro retains Te, Bi and Mo unlike many orogenic gold deposits (McCuaig and Kerrich 1998; Cassidy et al. 1998; Eilu et al. 1999; Goldfarb et al. 2005). However, this anomalous metal enrichment may (1) have been remobilised from the earlier magmatic–hydrothermal mineralisation and/or (2) result from the buffering of metamorphic fluids by evolved granite and granitic pegmatite at greater depth. Consequently, it is not necessarily indicative of input of magmatic–hydrothermal fluid. Also, the presence of hydrothermal biotite in the alteration assemblage associated with earlier mineralised sheeted veins at Bonikro but the lack of biotite in the subsequent alteration associated with the later phase of gold mineralisation imply a

drop in temperature over time, consistent with a change from magmatic–hydrothermal to orogenic gold mineralisation.

Regional gold metallogeny

Paleoproterozoic gold deposits of West Africa are not associated with any particular suite of plutonic rocks (Yonaka 1996; Goldfarb et al. 2017). Although granitoid-hosted gold deposits are known locally within West Africa (Oberthür et al. 1998; Allibone et al. 2002a, 2004), the brittle rheology of the granitoids compared with the adjacent volcanic and sedimentary country rocks is inferred to be the key factor that controlled the location of these deposits, rather than any genetic relationship between mineralisation and the host granitoids. In West Africa, only the Morila (McFarlane et al. 2011; King 2012) and Bonikro (this study) gold deposits have been genetically linked, at least in part, to the crystallisation of synorogenic plutons. At Morila, intrusion-related gold mineralisation occurred between 2098 ± 4 and 2074 ± 14 Ma, with the later date representing the orogenic gold overprint (McFarlane et al. 2011). This period coincides with emplacement of the Bonikro porphyritic granodiorite and both subsequent phases of gold mineralisation. The models for early intrusion-related gold mineralisation at Morila and Bonikro differ little from that envisioned for Phanerozoic intrusion-related gold deposits. Also, structural, timing, fluid and mineral paragenetic relationships suggest direct genetic links between high-K plutonism, magnetite-bearing endoskarn and exoskarn formation and gold mineralisation in nearby metasedimentary rocks in the Loulo and Sadiola districts in the eastern Kédougou-Kénieba inlier at ca. 2080–2060 Ma (Lawrence et al. 2013a, b; Lambert-Smith et al. 2016; Masurel et al. 2017c; Allibone et al. 2019). Although intrusion-related gold deposits are less common than orogenic gold deposits in West Africa, they comprise an economically important and mineralogically diverse group of deposits which formed late in the Eburnean orogeny throughout at least the western half of the Baoulé-Mossi domain.

Conclusions

The data presented herein suggests that the bulk of gold mineralisation in the Oumé-Féttékro Greenstone Belt occurred during a period of transcurrent tectonics late in the history of Eburnean tectono-magmatic activity, soon after the cessation of craton-wide compressional deformation (Agbahou, Houssou 2013; Houssou et al. 2017; Bonikro, Ouatarra 2015). Granitoids that host the Bonikro and Hiré gold deposits acted as favourable sites for fluid flow due to their brittle rheology compared with the adjacent supracrustal rocks, irrespective of their age, composition and oxidation state. Exploration strategies in the region should therefore aim, at least in part, to identify ore-controlling structures in granitoids or adjacent supracrustal rocks and predicting low mean stress areas where ore fluids may concentrate. The structural setting of the Bonikro gold deposit also indicates that the N- to NNE-trending brittle-ductile shear zones, which are discordant to the region-wide NE-trending structural grain, provide an important structural geometry in terms of predictive exploration. The data presented for the early gold phase at Bonikro is, however, inconsistent with a simple, classic orogenic gold deposit genesis. Gold mineralisation at Bonikro is suggested to reflect the overprint of late Eburnean orogenic gold mineralisation dated at 2074 ± 16 Ma on an earlier intrusion-related gold system linked to the local emplacement of a 2086 ± 4 Ma porphyritic granodiorite.

References

Abouchami W, Boher M, Michard A, Albarede F (1990) A major 2.1 Ga event of mafic magmatism in West Africa: an early stage of crustal accretion. J Geophys Res 95:17605–17629

Adadey K, Clarke B, Théveniaut H, Urien P, Delor C, Roig JY, Feybesse JL (2009) Geological map explanation—map sheet 0503 B at 1:100 000. Geol Survey Dep Ghana MSSP/2005/GSD/5a

Allibone AH, McCuaig TC, Harris D, Etheridge MA, Munroe S, Byrne D, Amanor J, Gyapong W (2002a) Structural controls on gold mineralization at the Ashanti gold deposit, Obuasi, Ghana. Econ Geol Spec Pub 9:65–93

Allibone AH, Teasdale J, Cameron G, Etheridge MA, Uttlev P, Soboh A, Appiah-Kubi J, Adanu A, Arthur R, Mamphey J, Odoom B, Zuta J, Tsikata A, Patave F, Famiyeh S, Lamb E (2002b) Timing and structural controls on gold mineralization at the Bogoso gold mine, Ghana, West Africa. Econ Geol 97:949–969

Allibone A, Hayden P, Cameron G, Duku F (2004) Paleoproterozoic gold deposits hosted by albite- and carbonate-altered tonalite in the Chirano district, Ghana, West Africa. Econ Geol 99:479–497

Allibone AH, Lawrence D, Scott J, Fanning M, Lambert-Smith J, Harbidge R, Vargas C, Turnbull R, Holliday J (2019) Paleoproterozoic gold deposits of the Loulo district, western Mali. Mineral Systems of West Africa (submitted)

Augustin J, Gaboury D, Crevier M (2016) The world-class Wona Kona gold deposit, Burkina Faso. Ore Geol Rev 78:667–672

Augustin J, Gaboury D, Crevier M (2017) Structural and gold mineralizing evolution of the world-class orogenic Mana district, Burkina Faso: multiple mineralizing events over 150 Ma. Ore Geol Rev 91:981–1012

Baratoux L, Metelka V, Naba S, Jessell MW, Grégoire M, Ganne J (2011) Juvenile Paleoproterozoic crust evolution during the Eburnean orogeny (ca. 2.2–2.0 Ga), western Burkina Faso. Precambrian Res 191: 18–45

Bessoles B (1977) Géologie de l'Afrique, le craton ouest-africain. Mémoire BRGM 88

Béziat D, Dubois M, Debat P, Nikiéma S, Salvi S, Tollon F (2008) Gold metallogeny in the Birimian craton of Burkina Faso (West Africa). J Afr Earth Sci 50:215–233

Béziat D, Siebenaller L, Salvi S, Chevalier P (2016) A weathered skarn-type mineralization in Ivory Coast: the Ity gold deposit. Ore Geol Rev 78:724–730

Birck JL, Barman MR, Capmas F (1997) Re-Os isotopic measurements at the femtomole level in natural samples. Geostand Geoanal Res 21(1):19–27

Block S, Jessell M, Aillères L, Baratoux L, Bruguier O, Zeh A, Bosch D, Caby R, Mensah E (2016) Lower crust exhumation during Paleoproterozoic (Eburnean) orogeny, NW Ghana, West African Craton: interplay of coeval contractional deformation and extensional gravitational collapse. Precambrian Res 274:82–109

Boher M, Abouchami W, Michard A, Albarede F, Arndt NT (1992) Crustal growth in West Africa at 2.1 Ga. J Geophys Res 97:345–369

Bosch D, Garrido CJ, Bruguier O, Dhuime B, Bodinier JL, Padron-Navarta JA, Galland B (2011) Building an island-arc crustal section: time constraints from a LA-ICP-MS zircon study. Earth Planet Sci Lett 309:268–279

Cassidy KF, Groves DI, McNaughton N (1998) Late-Archean granitoid-hosted lode-gold deposits, Yilgarn Craton, Western Australia: deposit characteristics, crustal architecture and implications for ore genesis. Ore Geol Rev 13:65–102

Compston W, Williams IS, Meyer C (1984) U–Pb geochronology of zircons from lunar breccia 73217 using a sensitive high mass-resolution ion microprobe. J Geophys Res 89:B252–B534

Creaser RA, Papanastassiou DA, Wasserburg GJ (1991) Negative thermal ion mass spectrometry of osmium, rhenium, and iridium. Geochim Cosmochim Acta 55(1):397–401

Daouda YB (1998) Lithostratigraphie et pétrologie des formations Birimiennes de Toumodi-Fettêkro, Côte d'Ivoire: implication pour l'évolution crustale du Paléoprotérozoique du craton Ouest-Africain. Ph.D. thesis, Université d'Orléans, France, Mémoire Geosciences 737, 191p

Davis DW, Hirdes W, Schaltegger U, Nunoo EA (1994) U-Pb age constraints on deposition and provenance of Birimian and gold-bearing Tarkwaian sediments in Ghana, West Africa. Precambrian Res 67: 89–107

Dia A, Van Schmus WR, Kröner A (1997) Isotopic constraints on the age and formation of Paleoproterozoic volcanic arc complex in the Kédougou inlier, eastern Senegal, West Africa. J Afr Earth Sci 24: 197–213

Doumbia S, Pouclet A, Kouamelan A, Peucat JJ, Vidal M, Delor C (1998) Petrogenesis of juvenile-type Birimian (Paleoproterozoic) granitoids in Central Côte-d'Ivoire, West Africa: geochemistry and geochronology. Precambrian Res 87:33–63

Dubé B, Gosselin P (2007) Greenstone-hosted quartz-carbonate vein deposits, In Goodfellow, W.D., ed., Mineral deposits of Canada: a synthesis of major deposit types, district metallogeny, the evolution of geological provinces, and exploration methods. Geological Association of Canada, Mineral Deposits Division Special Publication No. 5, pp. 49–73

Eglinger A, Thébaud N, Zeh A, Davis J, Miller J, Parra-Avila LA, Loucks R, McCuiag C, Belousova E (2017) New insights into the crustal growth of the Paleoproterozoic margin of the Archean Kénéma-Man domain, West African craton (Guinea): implications for gold mineral system. Precambrian Res 292:258–289

Eilu PK, Mathison CI, Groves D, Allardyce WJ (1999) Atlas of alteration assemblages, styles, and zoning in orogenic lode-gold deposits in a variety of host rock and metamorphic settings. The University of Western Australia, pub 30

Feybesse JL, Milési JP (1994) The Archaean/Proterozoic contact zone in West Africa: a mountain belt of décollement thrusting and folding on a continental margin related to 2.1 Ga convergence of Archaean cratons? Precambrian Res 69:199–227

Feybesse JL, Milési JP, Johan V, Dommanget A, Calvez JY, Boher M, Abouchami W (1989) La limite Archéen/Protérozoique inférieur d'Afrique de l'Ouest: une zone de chevauchement majeure antérieure à l'accident de Sassandra; l'exemple des régions d'Odiénné et de Touba (Côte d'Ivoire). C R Acad Sci Paris 309: 1847–1853

Feybesse JL, Billa M, Guerrot C, Duguey E, Lescuyer JL, Milesi JP, Bouchot V (2006) The paleoproterozoic Ghanaian province: geodynamic model and ore controls, including regional stress modeling. Precambrian Res 149:149–196

Fontaine A, Eglinger A, André-Mayer AS, Koumangdiwe A, Reisberg L, Siebenaller L, Le Mignot E, Ganne J, Poujol M (2017) Geology of the world-class Kiaka gold deposit, West African craton, Burkina Faso. J Afr Earth Sci 126:96–122

Fougerouse D, Micklethwaite S, Ulrich S, Miller J, Godel B, Adams DT, McCuaig TC (2017) Evidence for two stages of mineralization in West Africa's largest gold deposit: Obuasi, Ghana. Econ Geol 112: 3–22

Gasquet D, Barbey P, Adou M, Paquette JL (2003) Structure, Sr-Nd isotope geochemistry and zircon U-Pb geochronology of the granitoids of the Dabakala area (Côte d'Ivoire): evidence for a 2.3 Ga crustal growth event in the Paleoproterozoic of West Africa? Precambrian Res 127:329–354

Goldfarb RJ, Baker T, Dubé B, Groves DI, Hart CJR, Gosselin P (2005) Distribution, character, and genesis of gold deposits in metamorphic terranes. Econ Geol, 100th Anniversary Volume:407–450

Goldfarb RJ, André-Mayer AS, Jowitt SM, Mudd GM (2017) West Africa: the world's premier Paleoproterozoic gold province. Econ Geol 112:123–143

Hammond NQ, Robb L, Foya S, Ishiyama D (2011) Mineralogical, fluid inclusion and stable isotope characteristics of Birimian orogenic gold mineralization at the Morila mine, Mali, West Africa. Ore Geol Rev 39:218–229

Hart CJR (2005) Classifying, distinguishing and exploring for intrusion-related gold systems. The Gangue 87, 18p

Hart CJR, McCoy D, Goldfarb RJ, Smith M, Roberts P, Hulstein R, Bakke AA, Bundtzen TK (2002) Geology, exploration and discovery in the Tintina gold province, Alaska and Yukon. Econ Geol Spec Pub 9:241–274

Hein KAA (2010) Succession of structural events in the Goren greenstone belt (Burkina Faso): implications for West African tectonics. J Afr Earth Sci 56:83–94

Hirdes W, Davis DW (2002) U-Pb geochronology of Paleoproterozoic rocks in the southern part of the Kédougou-Kénieba inlier, Senegal, West Africa: evidence for diachronous accretionary development of the Eburnean Province. Precambrian Res 118:83–99

Hirdes W, Davis DW, Lüdtke G, Konan G (1996) Two generations of Birimian (Paleoproterozoic) volcanic belts in northeastern Cote d'Ivoire (West Africa), as demonstrated by precise U-Pb mineral dating: consequences for the "Birimian controversy". Precambrian Res 80:173–191

Houssou NN (2013) Etude pétrologique, structural et métallogénique du gisement aurifère d'Agbahou, Divo, Côte d'Ivoire. Ph.D. thesis, Université Felix Houphouet-Boigny, Côte d'Ivoire, 137p

Houssou NN, Allialy ME, Kouadio FJLH, Gnanzou A (2017) Structural control of auriferous mineralization in the Birimian: case of the Agbahou deposit in the region of Divo, Côte d'Ivoire. Int J Geosci 8:189–204

Jackson SE, Pearson NJ, Griffin WL, Belousova EA (2004) The application of laser ablation-inductively coupled plasma-mass spectrometry to in situ U-Pb zircon geochronology. Chem Geol 211:47–69

King K (2012) Geological, structural and mineralogical constraints on the evolution of the Morila gold deposit, South Mali, West Africa. Unpublished MSc. thesis, Kingston University, United Kingdom

Kirkland CL, Smithies RH, Taylor RJM, Evans N, McDonald B (2015) Zircon Th/U ratios in magmatic environs. Lithos 212-215:397–414

Lambert-Smith JS, Lawrence DM, Müller W, Treloar PJ (2016) Paleotectonic setting of the south-eastern Kédougou-Kénieba inlier, West Africa: new insights from igneous trace element geochemistry and U-Pb zircon ages. Precambrian Res 274:110–135

Lang JR, Baker T (2001) Intrusion-related gold systems: the present level of understanding. Mineral Deposita 36:477–489

Lawrence DM, Treloar PJ, Rankin AH, Harbidge P, Holliday J (2013a) The geology and mineralogy of the Loulo mining district, Mali, West Africa: evidence for two distinct styles of orogenic gold mineralization. Econ Geol 108:199–227

Lawrence DM, Treloar PJ, Rankin AH, Boyce A, Harbidge P (2013b) A fluid inclusion and stable isotope study at the Loulo mining district, Mali, West Africa: implications for multifluid sources in the generation of orogenic gold deposits. Econ Geol 108:229–257

Lawrence DM, Allibone AH, Chang Z, Meffre S, Lambert-Smith JS, Treloar PJ (2017) The Tongon Au deposit, northern Côte d'Ivoire: an example of Paleoproterozoic Au skarn mineralization. Econ Geol 112:1571–1593

Le Mignot E, Siebenaller L, Béziat D, André-Mayer AS, Reisberg L, Salvi S, Velasquez G, Zimmermann C, Naré A, Franceschi G (2017a) The Paleoproterozoic copper-gold deposits of the Gaoua district, Burkina Faso: superposition of orogenic gold on a porphyry copper occurrence? Econ Geol 112:99–122

Le Mignot E, Reisberg L, André-Mayer AS, Bourasse Y, Fontaine A, Miller J (2017b) Re-Os geochronological evidence for multiple Paleoproterozoic gold events at the scale of the west African craton. Econ Geol 112:145–168

Leake MH (1992) The petrogenesis and structural evolution of the early Proterozoic Fettekro greenstone belt, Dabakala region, NE Côte d'Ivoire. Unpublished Ph.D. thesis, Portsmouth, United Kingdom, 315p

Lebrun E, Thébaud N, Miller J, Ulrich S, Bourget J, Terblanche O (2016) Geochronology and lithostratigraphy of the Siguiri district: implications for mineralization in the Siguiri basin (Guinea, West Africa). Precambrian Res 274:136–160

Lebrun E, Miller J, Thébaud N, Ulrich S, McCuaig TC (2017) Structural controls on an orogenic gold system: the world-class Siguiri gold district, Siguiri basin, Guinea, West Africa. Econ Geol 112:73–98

Ledru P, Pons J, Milesi JP, Feybesse JL, Johan V (1991) Transcurrent tectonics and polycyclic evolution in the lower proterozoic of Senegal-Mali. Precambrian Res 50:337–354

Lemoine S (1982) Le décrochement ductile de Brobo, un linéament éburnéen majeur, son rôle possible dans l'orogénèse éburnéenne en Côte d'Ivoire. C R Acad Sci Paris 295:601–606

Lemoine S (1988) Evolution géologique de la région de Dabakala (NE de la Côte d'Ivoire), au Protérozoïque inferieur. Possibilités d'extension au reste de la Côte d'Ivoire et au Burkina Faso. Ph.D. thesis, Université de Clermont-Ferrand, France, 388p

Leube A, Hirdes W, Mauer R, Kese GO (1990) The Early Proterozoic Birimian Supergroup of Ghana and some aspects of its associated gold mineralization. Precambrian Res 45:139–165

Liégeois JP, Claessens W, Camara D, Klerx J (1991) Short-lived Eburnean orogeny in southern Mali. Geology, tectonics, U-Pb and Rb-Sr geochronology. Precambrian Res 50:111–136

Ludwig KR (2003) Isoplot 3.0; a geochronological toolkit for Microsoft Excel: Berkeley Geochro Centre Spec Pub 4, 70p

Ludwig KR (2009) Squid 2.50, a user's manual: unpublished report by Berkeley Geochronology Centre, California, USA, 95p

Masurel Q, Thébaud N, Miller J, Ulrich S, Hein KAA, Cameron G, Béziat D, Bruguier O, Davis JA (2017a) Sadiola Hill: a world-class carbonate-hosted gold deposit in Mali, West Africa. Econ Geol 112:23–47

Masurel Q, Thébaud N, Miller J, Ulrich S, Roberts MP, Béziat D (2017b) The Alamoutala carbonate-hosted gold deposit, Kédougou-Kénieba inlier, West Africa. Econ Geol 112:49–72

Masurel Q, Thébaud N, Miller J, Ulrich S (2017c) The tectono-magmatic framework to gold mineralisation in the Sadiola-Yatela gold camp and implications for the paleotectonic setting of the Kédougou-Kénieba inlier, West Africa. Precambrian Res 292:35–56

McCuaig TC, Kerrich R (1998) P-T-t-deformation-fluid characteristics of lode gold deposits: evidence from alteration systematics. Ore Geol Rev 12:381–453

McCuaig TC, Fougerouse D, Salvi S, Siebenaller L, Parra-Avila LA, Seed R, Béziat D, André-Mayer AS (2016) The Inata deposit, Belahouro district, northern Burkina Faso. Ore Geol Rev 78:639–644

McFarlane HB (2018) The geodynamic and tectonic evolution of the Paleoproterozoic Sefwi greenstone belt, West African craton. Ph.D. thesis, The University of Paul Sabatier, Toulouse, France, 265p

McFarlane CRM, Mavrogenes J, Lentz D, King K, Allibone A, Holcombe R (2011) Geology and intrusion-related affinity of the Morila gold mine, southeast Mali. Econ Geol 106:727–750

Milési JP, Ledru P, Feybesse JL, Dommanget A, Marcoux E (1992) Early Paleoproterozoic ore deposits and tectonics of the Birimian orogenic blet, West Africa. Precambrian Res 58:305–344

Milési JP, Feybesse JL, Pinna P, Deschamps Y, Kampunzu H, Muhongo S, Lescuyer JL, Le Goff E, Delor C, Billa M, Ralay F (2004) Geological map of Africa 1: 10,000,000, SIGAfrique project; in 20th conference of African geology, BRGM, Orléans, France

Mortimer J (1990) Evolution of early Proterozoïc Toumodi volcanic group and associated rocks, Ivory Coast. Ph.D. thesis, Portsmouth Polytechnic, United Kingdom, 244p

Mortimer J (1992a) Lithostratigraphy of the earlier Proterozoic Toumodi volcanic Group in Central Côte d'Ivoire: implications for Birimian stratigraphic models. J Afr Earth Sci 14:81–91

Mortimer J (1992b) The Kan River gneiss terrane of central Côte d'Ivoire: mylonitic remnants of an ancient magmatic arc? J Afr Earth Sci 15:353–357

Mortimer J (2016) Paleoproterozoic geology of the Toumodi area, Ivory Coast, 1:100,000. J Maps, doi: https://doi.org/10.1080/17445647.2016.1227732

Nasdala L, Hofmeister W, Norberg N, Martinson JM, Corfu F, Dörr W, Kamo SL, Kennedy AK, Kronz A, Reiners PW, Frei D, Kosler J, Wan Y, Götze J, Häger T, Kröner A, Valley JW (2008) Zircon M257 a homogeneous natural reference material for the ion microprobe U-Pb analysis of zircon. Geostand Geoanal Res 32:247–265

Newcrest Mining Limited (2012) Annual report: mineral resources and ore reserves, p 20

Newcrest Mining Limited (2016) Annual report: mineral resources and ore reserves, p 30

Oberthür T, Vetter U, Davis DW, Amanor JA (1998) Age constraints on gold mineralization and Paleoproterozoic crustal evolution in the Ashanti belt of southern Ghana. Precambrian Res 89:129–143

Olson SF (1989) Carte géologique de la concession de Hiré. BHP Minerals, archives SODEMI

Ouatarra Z (2015) Caractères lithostratigraphique, structural, géochimique, et mettalogénique du gisement d'or de Bonikro, sillon

Birimien de Oumé-Fettékro, centre sud de la Côte d'Ivoire. Ph.D. thesis, Université Felix Houphouet-Boigny, Côte d'Ivoire, 330p

Parra-Avila LA, Bourassa Y, Miller J, Perrouty S, Fiorentini ML, McCuaig TC (2015) Age constraints of the Wassa and Benso mesothermal gold deposits, Ashanti belt, Ghana, West Africa. J Afr Earth Sci 112:524–535

Parra-Avila LA, Kemp AIS, Fiorentini ML, Belousova E, Baratoux L, Block S, Jessell M, Bruguier O, Begg GC, Miller J, Davis J, McCuaig TC (2017) The geochronological evolution of the Paleoproterozoic Baoulé-Mossi domain of the southern West African Craton. Precambrian Res 300:1–27

Perrouty S, Aillères L, Jessell MW, Baratoux L, Bourassa Y, Crawford B (2012) Revised Eburnean geodynamic evolution of the gold-rich southern Ashanti belt, Ghana, with new field and geophysical evidence of pre-Tarkwian deformations. Precambrian Res 204-205:12–39

Perrouty S, Jessell MW, Bourassa Y, Miller J, Apau D, Parra-Avila LA, Le Mignot E, Velasquez G, Ganne J, Siebenaller L, Baratoux L (2016) Geological setting of the Wassa gold deposit, SW Ghana. Ore Geol Rev 78:687–691

Pigois JP, Groves DI, Fletcher IR, McNaughton NJ, Snee LW (2003) Age constraints ont Tarkwaian paleoplacer and lode-gold formation in the Tarkwa-Damang district, SW Ghana. Mineral Deposita 38:695–714

Pouclet A, Vidal M, Delor C, Simeon Y, Alric G (1996) Le volcanisme birimien du nord-est de la Côte d'Ivoire, mise en evidence de deux phases volcano-tecotniques distinctes dans l'évolution géodynamique du Paléoproterozoique. B Soc Geol Fr 167:529–541

Pouclet A, Doumbia S, Vidal M (2006) Geodynamic setting of the Birimian volcanism in central Ivory Coast (western Africa) and its place in the Palaeoproterozoic evolution of the Man Shield. B Soc Geol Fr 177:105–121

Robert F, Poulsen KH (2001) Vein formation and deformation in greenstone gold deposits. Econ Geol Rev 14:111–155

Schwartz MO, Melcher F (2003) The Perkoa zinc deposit, Burkina Faso. Econ Geol 98:1463–1485

Shirey SB, Walker RJ (1995) Carius tube digestion for low-blank rhenium-osmium analysis. Anal Chem 67:2136–2141

Smoliar MI, Walker RI, Morgan JW (1996) Re-Os ages of group IIA, IIIA, IVA, and IVB iron meteorites. Science 271(5252):1099–1102

Stacey JS, Kramers JD (1975) Approximation of terrestrial lead isotope evolution by a two-stage model. Earth Planet Sci Lett 26:207–221

Stern RA, Bodorkos S, Kamo SL, Hickman AH, Corfu F (2009) Measurement of SIMS instrumental mass fractionation of Pb isotopes during zircon dating. Geostand Geoanal Res 33:145–168

Sylvester PJ, Attoh K (1992) Lithostratigraphy and composition of 2.1 Ga greenstone belts of the West African Craton and their bearing on crustal evolution and the Archean-Proterozoic boundary. J Geol 100:377–393

Thomson JFH, Newberry RJ (2000) Gold deposits related to reduced granitic intrusions. Rev Econ Geol 13:377–400

Tshibubudze A, Hein KAA (2013) Structural setting of gold deposits in the Ouadalan-Gorouol volcano-sedimentary belt east of the Markoye shear zone, West African Craton. J Afr Earth Sci 80:31–47

Tshibubudze A, Hein KAA, Marquis P (2009) The Markoye shear zone in Burkina Faso. J Afr Earth Sci 55:245–256

Van Achterberg E, Ryan CG, Jackson SE, Griffin WL (2001) Data reduction software for LA-ICP-MS: appendix. In Sylvester, P.J. (eds.), Laser ablation-ICP-mass spectrometry in the earth sciences: principles and applications. Can Mineral, Short Course Series 29:239–243, Ottawa, Ontario, Canada

Vidal M, Gumiaux C, Cagnard F, Pouclet A, Ouattara G, Pichon M (2009) Evolution of a Paleoproterozoic "weak type" orogeny in the West African Craton (Ivory Coast). Tectonophysics 477:145–159

Völkening J, Walczyk T, Heumann KG (1991) Osmium isotope ratio determinations by negatic thermal ionisation mass spectrometry. Int J Mass Spectrom Ion Process 105:147–159

Wang X, Griffinn WL, Chen J, Huang P, Li X (2011) U and Th contents and Th/U ratios of zircon in flesic and mafic magmatic rocks: improved zircon-melt distribution coefficients. Acta Geol Sin 85:164–174

Wiedenbeck M, Allé P, Corfu F, Griffin WL, Meier M (1995) Three natural zircon standards for U-Th-Pb, Lu-Hf, trace element and REE analyses. Geostand Newslett 19:1–23

Williams IS, Buick IS, Cartwright I (1996) An extended episode of early Mesoproterozoic metamorphic fluid flow in the Reynolds Range, central Australia. J Metamorph Geol 14:29–47

Wingate MTD, Kirkland CL (2013) Introduction to geochronology information. Geological Survey of Western Australia Publication, 5p

Yacé I (1982) Etude géologique du volcanisme Eburnéen dans les parties centrale et méridionale de la chaine précambriénne de Féttékro. Rapport spécial du Ministère des mines, République de Côte d'Ivoire, 156p

Yao Y, Robb LJ (2000) Gold mineralization in Paleoproterozoic granitoids at Obuasi, Ashanti region, Ghana: ore geology, geochemistry and fluid characteristics. S Afr J Geol 103:255–278

Yao Y, Murphy PJ, Robb LJ (2001) Fluid characteristics of granitoid-hosted gold deposits in the Birimian terrane of Ghana: a fluid inclusion microthermometric and Raman spectroscopic study. Econ Geol 96:1611–1643

Yonaka BE (1996) Gold-bearing granitoids of southern Ghana, West Africa. Unpublished Ph.D. thesis, New Mexico Institute of Mining and Technology, U.S.A., 192p

Zitsmann A, Kiessling R, Loh G (1997) Geological, geophysical and geochemical investigations in the Bui Belt area in Ghana. Geol Jahrbuch, Reihe B 88:7–112